Observed Hurricane Wind Speed Asymmetries and Relationships to Motion and Environmental Shear

ERIC W. UHLHORN

NOAA/AOML/Hurricane Research Division, Miami, Florida

BRADLEY W. KLOTZ

Cooperative Institute for Marine and Atmospheric Studies, Rosenstiel School of Marine and Atmospheric Science, University of Miami, Miami, Florida

TOMISLAVA VUKICEVIC, PAUL D. REASOR, AND ROBERT F. ROGERS

NOAA/AOML/Hurricane Research Division, Miami, Florida

(Manuscript received 6 June 2013, in final form 19 November 2013)

ABSTRACT

Wavenumber-1 wind speed asymmetries in 35 hurricanes are quantified in terms of their amplitude and phase, based on aircraft observations from 128 individual flights between 1998 and 2011. The impacts of motion and 850–200-mb environmental vertical shear are examined separately to estimate the resulting asymmetric structures at the sea surface and standard 700-mb reconnaissance flight level. The surface asymmetry amplitude is on average around 50% smaller than found at flight level, and while the asymmetry amplitude grows in proportion to storm translation speed at the flight level, no significant growth at the surface is observed, contrary to conventional assumption. However, a significant upwind storm-motion-relative phase rotation is found at the surface as translation speed increases, while the flight-level phase remains fairly constant. After removing the estimated impact of storm motion on the asymmetry, a significant residual shear direction-relative asymmetry is found, particularly at the surface, and, on average, is located downshear to the left of shear. Furthermore, the shear-relative phase has a significant downwind rotation as shear magnitude increases, such that the maximum rotates from the downshear to left-of-shear azimuthal location. By stratifying observations according to shear-relative motion, this general pattern of a left-of-shear residual wind speed maximum is found regardless of the orientation between the storm's heading and shear direction. These results are quite consistent with recent observational studies relating western Pacific typhoon wind asymmetries to environmental shear. Finally, changes in wind asymmetry over a 5-day period during Hurricane Earl (2010) are analyzed to understand the combined impacts of motion and the evolving shear.

1. Introduction

Surface winds in tropical cyclones (TCs) are an important quantity to measure, particularly since the maximum wind speed in a TC defines the storm's intensity. Perhaps more important for practical purposes, however, is observing the full TC wind field, for example as quantified by integrated kinetic energy (Powell and Reinhold 2007). Storm surge flooding generated by landfalling TCs, which is also related to the size of the wind field (Irish et al. 2008), is responsible for far greater property damage and more deaths than result directly from wind. Storm surge forecasts therefore rely heavily on accurate forecasts of the surface wind field, including both the maximum wind speed (Xie et al. 2006) and asymmetries (Houston et al. 1999).

Observing the strong TC surface winds over the ocean has historically been limited, due to a relative paucity of observational platforms, instrumentation failures, and the inherent danger of low-level manned aircraft flight in extreme conditions. Indirect methods have been developed to infer surface winds from observations well above the TC boundary layer (Franklin et al. 2003; Powell et al. 2009), from the TC minimum central pressure (Knaff and Zehr 2007), and from satellite imagery (Velden et al.

Corresponding author address: Dr. Eric W. Uhlhorn, NOAA/AOML/Hurricane Research Division, 4301 Rickenbacker Cswy., Miami, FL 33149.
E-mail: eric.uhlhorn@noaa.gov

DOI: 10.1175/MWR-D-13-00249.1

2006), each with its own documented accuracy limitations. Direct surface wind data from global positioning system (GPS) dropwindsondes have greatly enhanced our understanding of boundary layer wind structures (Franklin et al. 2003; Powell et al. 2003; Kepert, 2006a,b; Schwendike and Kepert 2008), but spatial resolution limitations from the individual point measurements often prevent a detailed description of the full wind field in most cases (Landsea et al. 2004).

Recently, observations of the TC surface wind field have become available from stepped-frequency microwave radiometers (SFMRs; Uhlhorn et al. 2007), now installed on all operational and research hurricane reconnaissance aircraft flying in the Atlantic basin. The advantage of SFMR wind data is high spatial resolution radially with respect to the storm center, and relatively broad spatial coverage over the entire cyclone, since aircraft can traverse four quadrants of a storm in a matter of hours. Despite the improved surface wind sampling by SFMR, observing the peak 1-min surface wind in a TC remains elusive, since the maximum wind may be associated with transient eyewall vorticity maxima (EVM; Marks et al. 2008; Nolan et al. 2009) embedded within the spatially extensive eyewall region. A recent study has shown the highest observed SFMR wind over a single aircraft mission wind tends to underestimate the maximum 1-min wind speed by 6%–9% (Uhlhorn and Nolan 2012). However, the maximum wind speed is dominated by a relatively steady, and readily observable, symmetric wavenumber-0 (WN0) mean plus a wavenumber-1 (WN1) asymmetry (Vukicevic et al. 2014).

Numerous theoretical (e.g., Reasor et al. 2004; Riemer et al. 2010), observational (e.g., Reasor et al. 2000; Black et al. 2002; Corbosiero and Molinari 2002, 2003; Knaff et al. 2004; Cecil 2007; Reasor et al. 2013), and numerical (e.g., Wang and Holland 1996; Bender 1997; Frank and Ritchie 2001; Rogers et al. 2003; Wu et al. 2006; Braun and Wu 2007; Davis et al. 2008) studies of TCs in vertically sheared environments have described a typical asymmetric eyewall structure, in which the vortex tends to tilt roughly downshear, eyewall convection initiates in the downshear-right quadrant collocated with maximum boundary layer inflow, and precipitation is maximized downshear left. At extended radii, Hence and Houze (2008) described a process whereby rainbands outside of the radius of maximum winds (RMW) may be responsible for local horizontal wind maxima well above the boundary layer, and these maxima may project onto the low-wavenumber asymmetric structure, including horizontal winds. Following this description, Didlake and Houze (2009) presented evidence that downdrafts associated with tilted convective cores could transport momentum to the surface, possibly impacting the low-wavenumber near-surface horizontal wind field. Boundary layer wind asymmetries have also been attributed to storm translation (e.g., Shapiro 1983), in which differential friction across the storm yields convergence and forced vertical ascent; however, Corbosiero and Molinari (2003) cast some doubt on this result due to a preferential orientation of motion and shear directions. Within the context of sheared TCs, it should be noted that observational studies of horizontal wind asymmetric structure, especially near the surface, have been conducted far less frequently than have studies of convection and vertical motion asymmetries.

With recent improvements to observing system capabilities, more accurate parametric representations of TC surface winds may now be possible. Traditionally, earth-relative surface wind fields have been approximated as a simple translating axisymmetric vortex (e.g., Holland 1980), with a WN1 asymmetric component owing to the translational velocity (Georgiou 1985). This general practice of assuming that the asymmetry is maximized to the right of the storm track continues to this day, albeit with minor modifications (e.g., Xie et al. 2006; Hu et al. 2012), since consistent field observations have not routinely been available to quantify the amplitude and phase over a broad range of TC structures. Studies have suggested that there are several other interrelated processes that might be responsible for asymmetric boundary layer wind structure, including variations in surface friction (Shapiro 1983; Kepert 2001), the β effect (Ross and Kurihara 1992; Bender 1997), potential vorticity anomalies associated with asymmetric diabatic heating (Wang and Holland 1996), and environmental vertical shear (Rogers and Uhlhorn 2008). More recently, near-surface typhoon wind asymmetries have been examined using mesoscale analysis fields (Ueno and Kunii 2009) and National Aeronautics and Space Administration (NASA) Quick Scatterometer (QuikSCAT) data (Ueno and Bessho 2011). Both of these studies emphasized a preferential left-of-shear storm-relative surface tangential wind asymmetry that was amplified when the vertical shear was stronger.

Surface wind analysis algorithms have been developed to provide guidance for forecasters, such as axisymmetric parametric models, variants based on these simple models, and near-real-time two-dimensional field analyses based on observations in the TC environment. Parametric models typically represent the wind field based on a few input parameters, while more sophisticated analyses range from objective statistical representations such as are utilized in H*Wind (Powell and Houston 1996; Powell et al. 2010) and variational fitting approaches (Knaff et al. 2011; Bell et al. 2012), as well as

data assimilative models with dynamical constraints (e.g., Aksoy et al. 2013). To address the issue of the maximum resolvability of the surface wind field from standard aircraft observations, a semispectral analysis algorithm is developed to quantify the TC surface wind structure for a sample of Atlantic basin hurricanes (35) obtained on 128 aircraft missions over the past several years (1998–2011). In addition, such an analysis is easily applied to high-resolution numerical forecast model wind fields for scale-consistent comparison with observations (Vukicevic et al. 2014).

The purpose of this study is to document low-wavenumber surface wind asymmetries in hurricanes, and their relationships to motion and environmental shear, focusing particular attention on asymmetries at the radius of maximum wind. Relationships between surface and flight-level (typically, 700 mb) asymmetries are also developed. In section 2, the data sample and processing techniques are discussed, and the analysis methodology is developed. Section 3 presents the analysis results, composited separately relative to motion and shear (both magnitude and direction), and the evolution of asymmetries in an individual case study of Hurricane Earl (2010) is examined in section 4. In section 5, implications for the results on the coupling of kinematic and convective asymmetries are discussed, and finally section 6 summarizes the results and suggests directions for future study.

2. Data and methodology

a. Sample hurricanes

SFMR surface and flight-level wind speed data obtained from 128 aircraft missions in 35 hurricanes between 1998 and 2011 are utilized to construct wind field analyses. Figure 1 shows geographic locations of storms at the time of analysis. Storms range from categories 1 through 5 on the Saffir–Simpson hurricane scale, and cover a broad range of storm motion speeds and shear magnitudes (Fig. 2). Storm intensity in terms of maximum wind speed (V_{max}) and storm motion speed (V_{storm}) are obtained from the Hurricane Database version-2 (HURDAT2) derived from the National Hurricane Center's (NHC) best track dataset (Jarvinen et al. 1984) corresponding to the time of aircraft observation. The 850–200-mb environmental vertical shear (V_{shr}) obtained from the Statistical Hurricane Intensity Prediction Scheme (SHIPS; DeMaria et al. 2005) reanalysis database (containing years 1982–2012) is the mean value over the 0–500-km radius centered on the storm after removing the vortex. Table 1 lists hurricanes and corresponding numbers of aircraft missions.

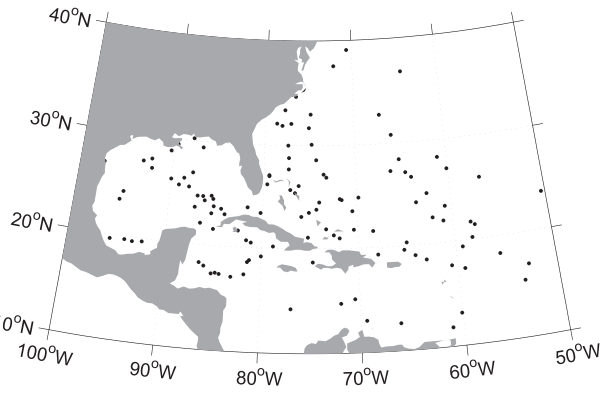

FIG. 1. Geographical locations of hurricanes analyzed for this study.

Where distinctions are necessary, cardinal directions are identified either in an earth-relative coordinate as north (N), east (E), south (S), and (W); in a storm-heading-relative coordinate as forward of motion (FM), right of motion (RM), behind motion (BM), and left of motion (LM); or in a shear-heading-relative coordinate as downshear (DS), right of shear (RS), upshear (US), and left of shear (LS). In all cases, an angle of 0° is directed either N, FM, or DS, and angles are measured positive clockwise. For motion and shear-relative angles, the cyclic ambiguity point is set at ±180° throughout.

Since asymmetric wind structure theoretically results from storm motion (Shapiro 1983; Kepert 2001), and possibly environmental shear (Rogers and Uhlhorn 2008; Ueno and Kunii 2009), the relationship between motion and shear is considered. Corbosiero and Molinari (2003) analyzed this relationship to understand the relative importance of motion and shear on convective asymmetries based on lightning flash spatial distribution. Here, this shear-relative motion analysis methodology is followed, with some minor convention changes for convenience. Frequency distributions of motion and shear directions (headings), and the difference between the two, are shown in Fig. 3 for the analyzed sample. The sample vector-mean hurricane travels at $V_{storm} = 5.1\,m\,s^{-1}$, heading $\theta_{storm} = 320°$ (toward NW; Fig. 2a). The environmental shear is more broadly distributed with a vector mean of $V_{shr} = 6.5\,m\,s^{-1}$, heading $\theta_{shr} = 51°$ (from SW; Fig. 2b). Subtracting the shear direction from the motion direction (Fig. 2c) results in a typical storm motion that is downshear left [mean $(\theta_{storm} - \theta_{shr}) = -36°$]. Note that the scalar mean directional difference does not generally equate to the difference between vector means. Corbosiero and Molinari (2003) also reported a typical downshear-left motion direction for their sample, most often between −45° and −30° relative to the shear direction. For reference, over the entire 1982–2012

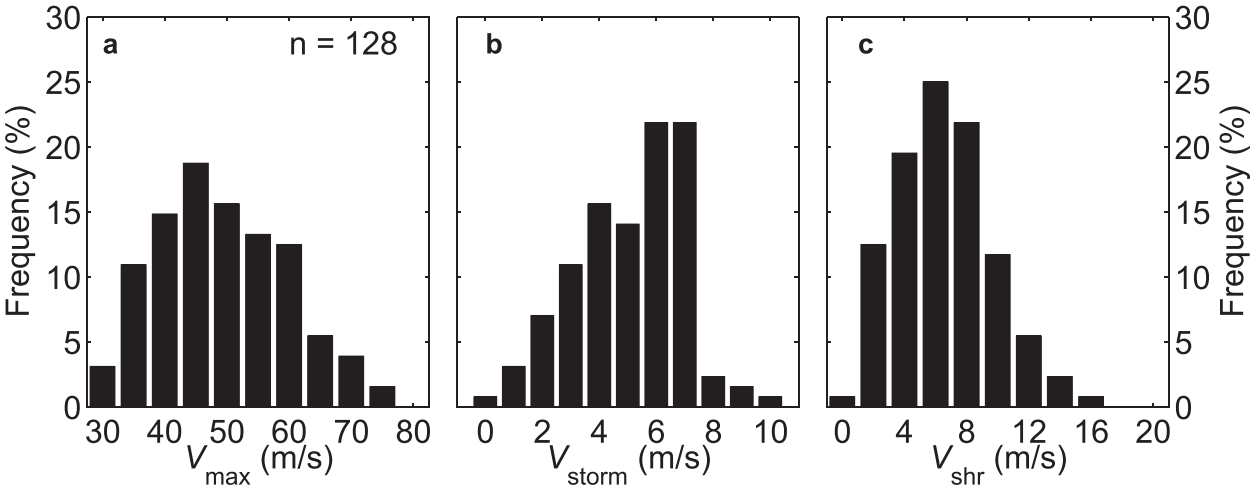

FIG. 2. Frequency distributions of (a) TC intensity V_{max}, (b) storm motion speed V_{storm}, and (c) 850–200-mb environmental shear magnitude V_{shr} for the $n = 128$ storm sample. All quantities are in units of $m\,s^{-1}$.

SHIPS database, the mean hurricane travels at $V_{storm} = 6.1\,m\,s^{-1}$ with heading $\theta_{storm} = 347°$, and experiences shear of $V_{shr} = 8.1\,m\,s^{-1}$ heading $\theta_{shr} = 67°$, suggesting the sample analyzed here is a reasonable representation of North Atlantic hurricanes in general.

b. SFMR surface wind processing

The SFMR measures brightness temperatures at six frequencies in the microwave C band, from which the surface wind speed is retrieved. A geophysical model (Uhlhorn and Black 2003; Uhlhorn et al. 2007), which relates surface emission to wind speed, has been developed with the aid of in situ observations by GPS dropwindsondes. Wind observations are computed every 30 s, and each value corresponds to the highest 10-s-average wind over consecutive 30-s intervals, as is produced for real-time operations. This peak 10-s value along the flight track represents a 1-min-average value at a fixed point (Powell et al. 1991; Uhlhorn and Nolan 2012).

Recent studies have examined SFMR winds to reveal some minor deficiencies under specific situations. Powell et al. (2009) analyzed differences in SFMR wind speeds relative to dropwindsondes as a function of storm-motion-relative azimuthal angle, and found a small residual asymmetry of amplitude $\sim 2\,m\,s^{-1}$. A similar result was found for a smaller sample by Uhlhorn and Black (2003). It was hypothesized that this bias was due to sea state asymmetry related to variable wind–wave interactions around a storm. This bias correction [Eq. (1) in Powell et al. (2009)] is applied to the winds in this study.

The SFMR is designed to measure surface winds in all-weather conditions, including heavy precipitation. However, retrieval accuracy has been shown to be degraded in weak-to-moderate winds coupled with heavy precipitation. In particular, winds are typically overestimated in such conditions. A recent project funded by the U.S. Weather Research Program Joint Hurricane Testbed quantified this bias over the expected range of winds and rain rates in hurricanes. In general, the bias was found to be largest at the weakest wind speeds and heaviest precipitation, and diminishes as surface winds increase. At minimal hurricane-force winds ($V_{max} = 33\,m\,s^{-1}$), the mean bias is not more than $\sim 2.5\,m\,s^{-1}$, and decreases to near zero by $\sim 50\,m\,s^{-1}$. A bias correction function (Klotz and Uhlhorn 2013, manuscript submitted to *Mon. Wea. Rev.*) based on these results is applied to the SFMR surface wind data.

TABLE 1. Hurricanes and number of aircraft missions (in parentheses) analyzed in this study. Storms begin in 1998 corresponding to the initial availability of SFMR data of documented accuracy.

Year	Storm (No. of flights)
1998	Bonnie (3), Earl (1), Georges (2)
1999	Bret(1), Dennis (2), Floyd (2), Lenny (1)
2001	Humberto (2)
2002	Isidore (1), Lili (2)
2003	Fabian (1), Isabel (2)
2004	Frances (6), Ivan (6), Jeanne (1)
2005	Katrina (4), Rita (5), Wilma (1)
2006	Helene (2)
2007	Felix (3)
2008	Dolly (1), Gustav (7), Ike (8), Paloma (3)
2009	Bill (5)
2010	Alex (1), Danielle (2), Earl (18), Igor (6), Karl (3), Paula (1), Tomas (3)
2011	Irene (14), Katia (1), Maria (1), Rina (6)
Total	35 (128)

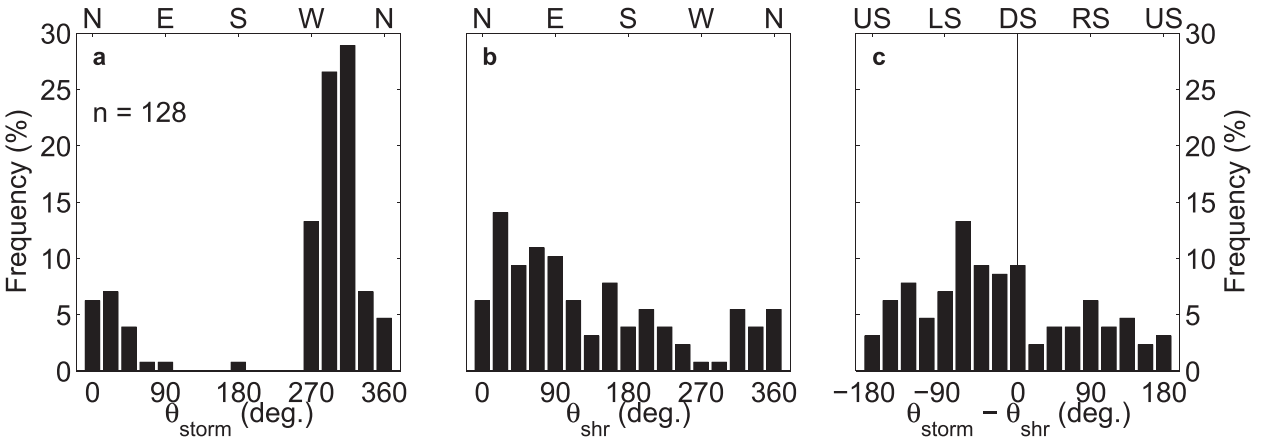

FIG. 3. Frequency distributions of (a) storm motion direction θ_{storm}, (b) 850–200-mb environmental shear direction θ_{shr}, and (c) shear-direction-relative storm motion $\theta_{storm} - \theta_{shr}$. All quantities are in degrees azimuth. In (a) and (b), 0° is north. In (c), 0° indicates the downshear motion direction, and angles >0° or <−180° indicate motion to the right of the shear direction.

c. *Objective wind field analysis*

Like aircraft flight-level winds, surface wind speeds measured by SFMR are obtained periodically at high frequency [typically, 1 Hz; Uhlhorn et al. (2007)] along the flight track. Historically, hurricane reconnaissance flight patterns have consisted of radial legs to and from the storm center (e.g., Sheets 2003), a practice that generally continues today. Thus, data sampling is dense in the radial dimension, but comparatively fewer data in the azimuthal dimension are available, especially as radius increases, with the exception of downwind legs connecting successive radial legs. From this type of sampling pattern, a semispectral analysis is a convenient representation of the wind field, with the radial dimension represented in physical space and the azimuthal dimension in wavenumber space.

The analysis system considers the scales of quantities resolved by the observation network (i.e., aircraft). Considering the SFMR radiative footprint at typical aircraft ground speeds, each wind observation represents an approximately 3-km spatial scale along the flight track, and around 1 km in the cross-track dimension (Uhlhorn and Nolan 2012). Since each observation is spaced 30 s (~3.5 km) apart, there is only around 0.5 km of latency between observations.

The observation scales lead to the design of the analysis field. From an individual flight, each radial leg (inbound or outbound from the center) is identified. For example, a single ''figure 4'' pattern consists of four individual radial legs. For each leg, an RMW (R_{max}) is found at both the surface and flight levels, and used to normalize the observed distance r from the storm center ($r^* = r/R_{max}$). Each radial leg is then interpolated onto a normalized grid, whose spacing (Δr^*) depends on the average RMW to maintain consistency with the approximately 3-km radial sampling. A similar methodology was used to develop composite radial profiles of flight-level winds (Mallen et al. 2005). As an example, an average RMW of 30 km suggests $\Delta r^* = 0.1$. Since radial legs typically extend 105 n mi (~194 km) from the storm center, wind observations in this example would be available radially outward to $r^* \simeq 6.5$. The advantage of this method is that the WN0 component is maximized at $r^* = 1$ by eliminating errors due to storm-center location uncertainty. A disadvantage is that real asymmetries resulting from elliptical vortex structure or wind center displacement are not captured.

An example of observational data input into the analysis is shown in Fig. 4, from a flight in Hurricane Katrina on 28 August 2005. The georeferenced flight track (Fig. 4a) consists of a rotated figure-4 pattern (with one repeated final fifth radial leg), in which eight azimuths are sampled over the flight. Surface and 700-mb flight-level wind speeds over the approximately 9-h flight (Fig. 4b) show the five eye penetrations. For analysis purposes, the first four radial inbound–outbound legs are used (Fig. 4c). Wind speeds are plotted as a function of normalized radial distance from the storm center (Fig. 4d), based on the storm track from NHC supplemented with additional storm-center locations provided by the Hurricane Research Division, and RMWs determined for each of the legs at both the surface and flight levels.

The analysis methodology has been previously applied to Hurricane Rita (2005) for winds at $r^* = 1$ (Rogers and Uhlhorn 2008) and, here, is generalized to all radii at which data are routinely available. Based on the storm center found from the wind speed minimum for each pass, the azimuthal angle λ measured clockwise

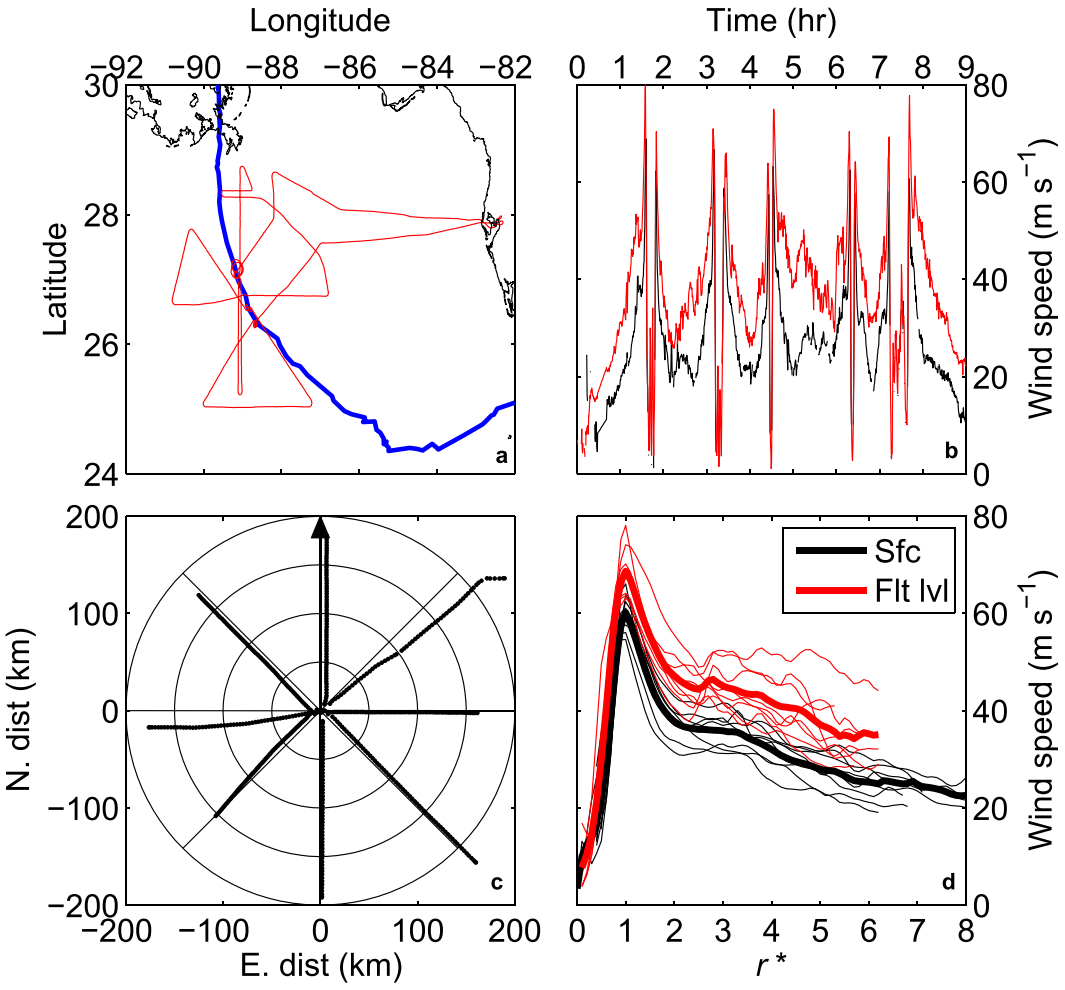

FIG. 4. (a) National Oceanic and Atmospheric Administration (NOAA) WP-3D flight track (red) and Hurricane Katrina storm track (blue), (b) surface (black) and 700-mb flight-level (red) wind speed time series for the flight duration, (c) observation locations relative to moving storm center, and (d) surface (black) and flight-level wind speeds as functions of normalized radial distance (r^*). In (c), the arrow points north.

relative to the storm-motion direction is computed for each observation. These angles are also interpolated onto the same normalized radial (r^*) grid. At each normalized radius, a set (typically four, six, or eight, depending on flight pattern) of wind speed observations at corresponding azimuth angles is obtained. A harmonic function of the form

$$S(r^*,\lambda) = A_{s0}(r^*) + A_{s1}(r^*)\cos[\lambda - \phi_{s1}(r^*)] + \epsilon \qquad (1)$$

is fit to the observations using a least squares method. At each radius, a set of three parameters [WN0 axisymmetric mean (A_{s0}), WN1 asymmetric amplitude (A_{s1}), and phase (ϕ_{s1})] describes the WN0 + 1 two-dimensional wind field S at either the surface or flight level, with an associated residual error ϵ. As a matter of the least squares principle, each parameter itself has an associated error, which is also computed. The maximum WN0 + 1 wind speed is defined to be located at $(r^*,\lambda) = (1,\phi_{s1})$. As a result, the wind fields at the surface and flight level may be reconstructed from the coefficients as a function of normalized radius. Figure 5 shows WN0 + 1 wind fields for the Hurricane Katrina descriptive example, where the mean RMWs at the surface (24.5 km) and flight level (31.1 km) are used in the conversion back to the physical radial distance.

d. Analysis limitations

In some situations, for example when a cyclone is being investigated for potential development (an INVEST mission), the semispectral analysis method described above does not lend itself to accurate description of the wind field. In such cases, the vortical wind field structure is perhaps not well defined, and the flight pattern may

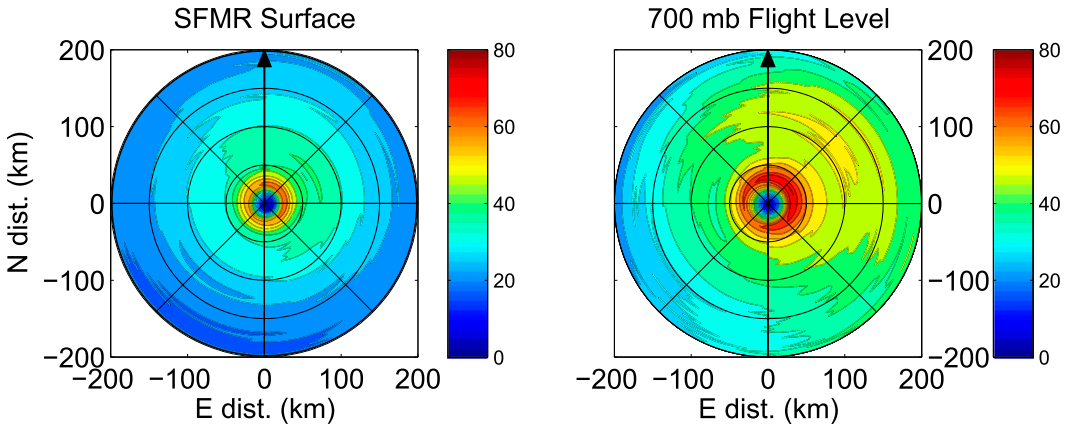

FIG. 5. (left) Surface and (right) flight-level WN0 + 1 wind speed analysis for Hurricane Katrina on 28 Aug 2005. The arrow in each panel points north. Wind speed units are in m s^{-1}.

not consist of regularly spaced radial legs that are convenient for a polar analysis. It may be more appropriate to apply a traditional successive-correction objective analysis (e.g., Barnes 1964) or optimal interpolation (e.g., Bergman 1979) in these situations, from which the WN0 + 1 could subsequently be extracted. To avoid these potential issues, analyses are restricted to TCs minimally of hurricane strength in this study.

For a number of reasons, the analysis procedure is truncated at WN1. Often, reconnaissance missions consist of one single figure-4 pattern, which provides observations at four azimuthal locations. To unambiguously determine the WN0 mean, as well as WN1 amplitude and phase, a minimum of three observations around the storm is required, in which case WN1 is the highest resolvable asymmetric component. Second, the analysis is synoptic in nature, as temporal evolution of the field over the observation period (typically a few hours) is not considered. Higher-order components are often not stationary, for example, embedded mesocyclones (e.g., Kossin and Schubert 2001). These features generally propagate around the eyewall relative to the mean flow and may quickly grow and decay; therefore, the amplitude and phase of these features cannot be estimated with a high degree of confidence. Also, since their propagation is not likely to coincide with the aircraft sampling, their energy may be aliased into lower wavenumbers.

As an example of the potential impact of higher-order harmonics on a WN0 + 1 analysis, the previous example from Katrina is examined further. With eight wind observations around the eyewall over the flight, theoretically up to WN3 may be resolved assuming a stationary field composed of linear, noninteractive spectral components. A Fourier decomposition is carried out to third-order harmonic at the RMW to quantify the impact on the WN1 estimate when higher-order terms are considered. Figure 6 shows three representations of the wind speed at $r^* = 1$: wavenumbers 0 through 1 (WN0 + 1), wavenumbers 0 through 2 (WN0 + 1 + 2), and wavenumbers 0 through 3 (WN0 + 1 + 2 + 3). As higher harmonics are considered, the fit to the observations improves. However, the WN1 amplitude A_1 grows, and the phase ϕ_1 shifts. The amplitude growth is contrary to expectations under an energy-conservation constraint, since attributing total energy progressively to higher harmonics should result in a decrease in lower-harmonic energy. It is possible that temporal aliasing of nonstationary harmonics, for example, as manifested in eyewall mesocyclones, is artificially contributing to the estimated WN1 asymmetry.

This example is rather extreme as hurricanes with similar inner-core annular structure (Knaff et al. 2003) have been shown to be particularly supportive of energetic higher-order, subvortex-scale embedded circulations. Still, in this particular case the maximum WN0 + 1 is ~93% of the highest observed surface wind speed of 70.1 m s^{-1}, indicating its dominant contribution. It is anticipated that such artifacts are not generally as detrimental to the low-wavenumber analysis. Future instrumentation such as the Hurricane Imaging Radiometer (HIRAD) on NASA's GlobalHawk aircraft (Braun et al. 2013), alternative sampling patterns, and high-resolution modeling studies could help elucidate the impact of high-wavenumber components on a low-wavenumber wind field analysis.

3. Results

a. Mean and asymmetric structure versus radius

Composite mean and asymmetric wind fields at the surface and flight level are constructed from the 128

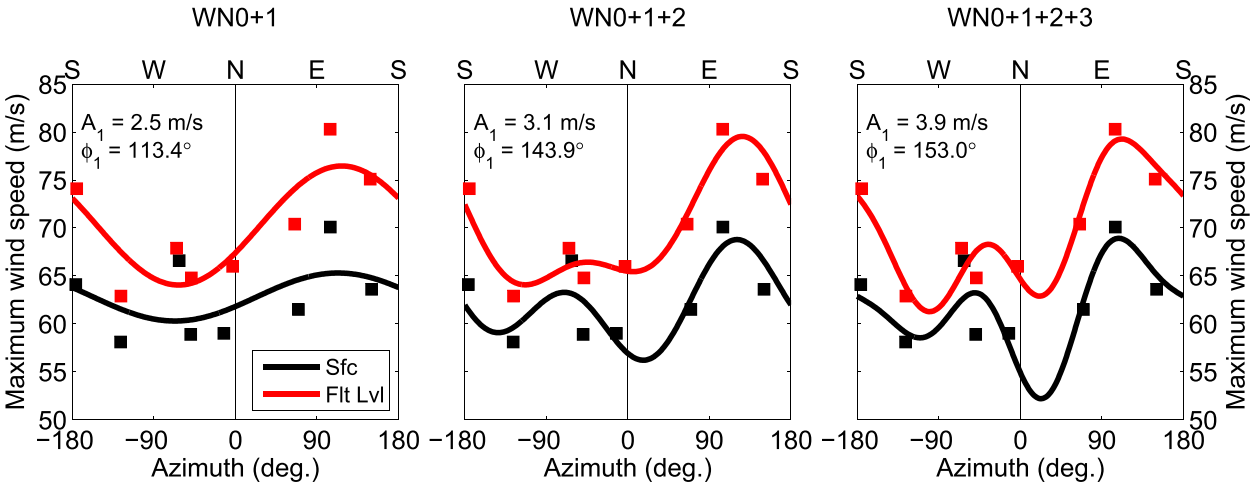

FIG. 6. Maximum observed wind speed along each of eight radials (solid squares) at the surface (black) and 700-mb flight level (red) in Hurricane Katrina plotted as functions of azimuth angle (°) clockwise from north, and least squares harmonic fits to observations. From left to right, fits contain WN0 + 1, WN0 + 1 + 2, and WN0 + 1 + 2 + 3. Surface WN1 component amplitude (A_1, m s^{-1}) and phase (ϕ_1, °) are labeled for each panel.

analyses. The vast majority (>90%) of flight-level wind data are obtained at the 700-mb (~3 km) standard reconnaissance altitude, and all flights are between 2.4 and 3.6 km, or ~760 and ~640 mb, respectively. Symmetric mean (WN0), and asymmetric wavenumber-1 (WN1) amplitude (A_{s1}) and phase (ϕ_{s1}), are plotted as functions of normalized radius (r^*) based on the RMWs at either the surface or flight level, as necessary (Fig. 7). Therefore, the wind maxima at both the surface and flight levels are located at $r^* = 1$, although physically the flight-level peak is often found radially outward of the surface peak as a result of eyewall slope (Powell et al. 2009; Stern and Nolan 2009).

Outside of the inner core ($r^* \geq 2$), the average surface WN0 wind speed is around 75%–80% of the flight-level value, and this ratio increases to around 90% at the surface RMW (Fig. 7a). Similar results have previously been computed by analytical models (Kepert 2001), and have been observed for reductions of maximum flight-level winds to the surface (Franklin et al. 2003). The composite axisymmetric surface wind decays at a faster rate radially outward from the RMW ($\sim r^{*-0.35}$) than at flight level ($\sim r^{*-0.25}$), although there is significant case-to-case variability that is possibly due to other factors, including intensity (Mallen et al. 2005), intensity tendency, latitude, and translation speed (Holland et al. 2010). Radially inward of the surface RMW, the surface wind speed approaches 100% of the flight-level wind, due to eyewall slope, as is typically observed (e.g., Powell et al. 2009, Fig. 1).

Averaged over the sample, the WN1 asymmetry amplitude (Fig. 7b) is around 50% higher at the flight level than at the surface, particularly between $1 < r^* < 5$. At greater radii, the amplitude difference becomes statistically insignificant. Radially inward of the RMW, there is an apparent increase in surface asymmetry amplitude. However, the asymmetry becomes more difficult to diagnose here, due to both error in the reference storm center location, as well as possible higher-order nonstationary asymmetries being aliased into the low-wavenumber structure. Thus, the accuracy of asymmetry results inside of the RMW is somewhat suspect at present.

The WN1 asymmetry phase is defined here as the storm-motion-relative azimuthal location of the asymmetry maximum (i.e., where $\lambda = \phi_{s1}$). The phase (Fig. 7c) is generally located close to directly right of storm motion at the flight level, and the surface WN1 maximum is typically found in the right-front quadrant, ~40° to the right of the storm motion as previously found in a smaller sample (Uhlhorn et al. 2007). Therefore, there is generally an upwind rotation of wind maximum from the surface to the flight level. As for the amplitude, the apparent downwind phase rotation at both the flight level and the surface inside of the RMW may be artificial.

b. Asymmetry dependence on storm motion

The dependence of surface and flight-level wind asymmetries on storm motion is estimated, focusing on the asymmetries at the RMW. Fourier coefficients (A_{s1} and ϕ_{s1}) derived from the 128 analyses are plotted as functions of V_{storm} (Fig. 8). Linear regression fits ($a + bV_{storm}$) are computed to estimate the motion dependence. The WN1 asymmetry dependence is apparently manifested in different ways at the surface and at flight level. The surface A_{s1} has little, if any, dependence

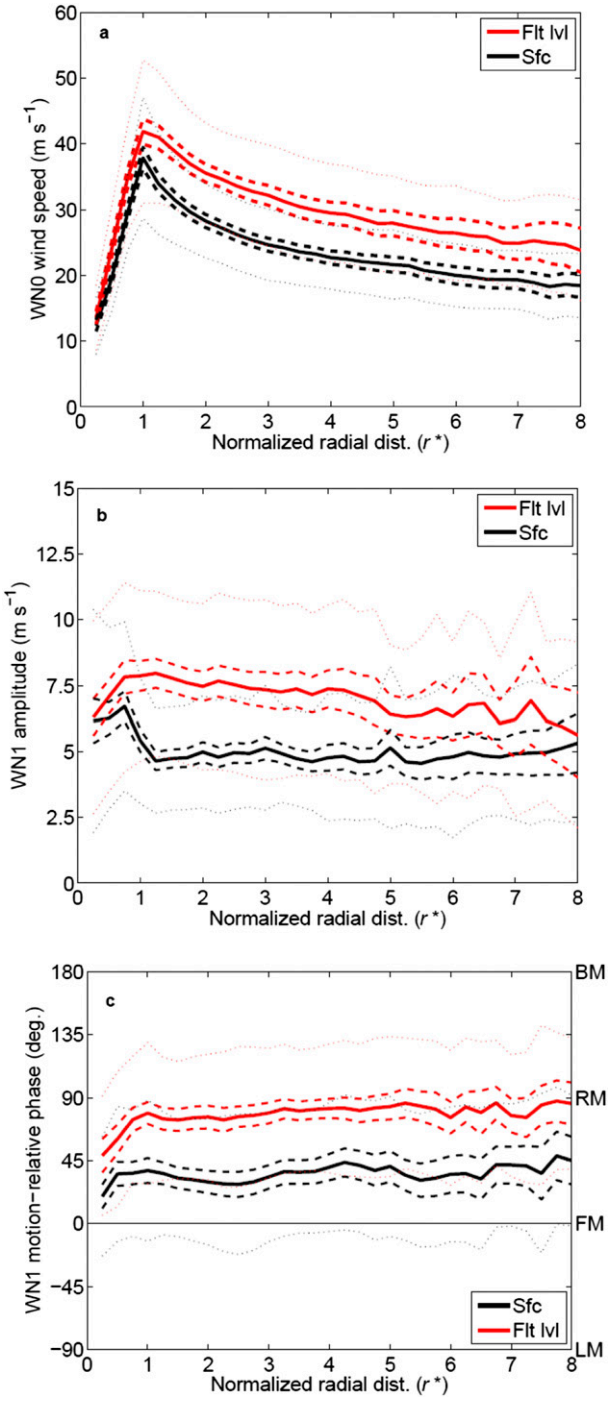

FIG. 7. Composite (a) WN0 wind speed ($m\,s^{-1}$), (b) WN1 amplitude ($m\,s^{-1}$), and (c) WN1 motion-relative phase (°) at the surface (black) and flight level (red) as functions of normalized radius (r^*). Solid lines are means for the $n = 128$ sample, thick dashed lines are 95% confidence intervals on the means, and dotted lines are one standard deviation.

on storm motion speed, and ϕ_{s1} has a small, but statistically significant, tendency to rotate upwind as motion increases. At flight level, a large increase in amplitude with V_{storm} is found, with little phase shift as motion increases. Table 2 lists the coefficients of linear fits plotted in Fig. 8.

It has typically been assumed that the surface wind field becomes more asymmetric as storm motion increases, and an extrapolation of flight-level winds to the surface would reflect this. For example, parametric wind models used for forcing storm surge predictions often simply add the storm motion vector to the symmetric wind field, resulting in an amplitude $A_{s1} = V_{storm}$, with constant phase $\phi_{s1} = 90°$. Over the hurricane sample assembled here, this would appear to be an incorrect assumption. However, due to an asymmetry *phase shift*, an anemometer measuring the wind speed at a location exactly 90° to the right of motion at the RMW would indicate a higher wind speed for a faster-moving storm for the same WN0 + WN1 wind.

Although the SFMR has assumed a prominent role in helping forecasters diagnose hurricane intensity when aircraft reconnaissance data are available, flight-level winds remain an important tool for determining intensity, as well as providing a basis for detecting occasional anomalous SFMR behavior. In the absence of direct surface wind data during hurricanes, near-surface winds have been estimated from flight-level wind data using a standard wind-reduction factor (Franklin et al. 2003). Powell et al. (2009) examined the relationship between observed surface and flight-level maximum wind speeds using SFMR wind data within a composite framework and found that the ratio of surface-to-flight-level wind (simply, "ratio") was typically larger to the left of storm motion. In this previous study, the amplitude of the WN1 ratio asymmetry was estimated to be approximately 5%; that is, the ratio was ~10% larger on the left side of the storm than on the right side. Furthermore, a small asymmetry amplification with increased storm motion speed was found, although no indication of statistical significance was provided.

Wind speed ratio asymmetries are examined at the RMW for the 128 sample cases. The WN0 + 1 asymmetry model [Eq. (1)] is fit to the observed ratio as a function of the azimuth to estimate amplitude (A_{r1}) and phase (ϕ_{r1}), and frequency histograms are plotted in Fig. 9. On average, the maximum ratio is found in the left-front quadrant relative to storm motion (mean $\phi_{r1} = -69°$), but does not significantly rotate with increased storm motion speed (not shown). The mean asymmetry amplitude is $A_{r1} = 11\%$, and also does not change significantly with storm motion speed.

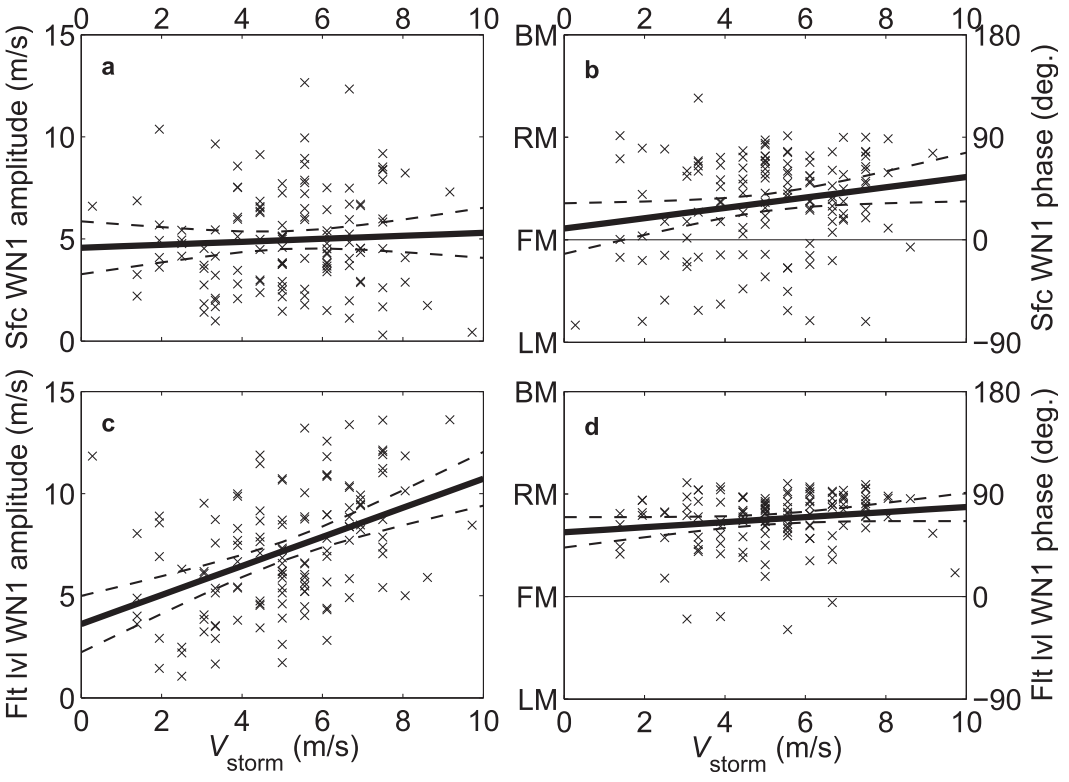

FIG. 8. Surface WN1 (a) amplitude and (b) phase, and flight-level WN1 (c) amplitude and (d) phase at the RMW for each of the 128 analyses, as a function of storm motion speed (V_{storm}, m s^{-1}). Asymmetry amplitudes are in m s^{-1}, and storm motion-direction phase angles are in °. Linear regressions (solid lines) and 95% confidence intervals for the fits (dashed lines) are also shown.

c. *Asymmetry dependence on environmental shear*

The potential impact of environmental shear on wind asymmetries at the RMW is examined after removing the storm-motion-induced asymmetry. Customarily, storm-relative winds are computed by vector subtraction of the storm motion from the wind, which is not directly possible here since the SFMR does not observe wind direction. To avoid this problem, the empirically derived asymmetries in Table 2 are first subtracted from the wind speeds, and data are then rotated to a shear-direction-relative coordinate system, where $\lambda = 0°$ is now oriented in the DS direction. The harmonic least squares fitting proceeds as before to estimate Fourier coefficients describing the asymmetry as a function of environmental shear magnitude (V_{shr}). Figure 10 shows the coefficients at both the surface and flight level.

After removing the estimated motion-induced asymmetry, a dependence on shear magnitude is found, particularly at the surface. The amplitude and phase dependencies (Fig. 10) indicate the most significant impact of environmental shear on the surface wind asymmetry is a cyclonic upshear rotation of the wind maximum—from the DS to LS locations—with increasing shear magnitude. A small rotation is also found at flight level, but the trend is not statistically significant. The average asymmetry amplitudes at both surface and flight level are around 3–5 m s^{-1}, and are statistically significant from zero at the 95% confidence level. The residual shear-relative amplitude is a significant component of the total observed asymmetry, which previously was found to be ~5 m s^{-1} at the surface. Table 3 lists the linear regression coefficients for the fits shown in Fig. 10.

As was done for storm motion, the impact of environmental shear on residual surface wind reduction from flight level is examined (Fig. 11). For this sample,

TABLE 2. Linear regression coefficients for asymmetry vs motion speed relationships [$(A_1, \phi_1) = a + bV_{storm}$] at surface and flight levels. Values are estimates and 95% confidence intervals, with boldface type indicating statistical significance. Phase angles are clockwise relative to storm motion.

	Surface		Flight level	
	a	*b*	*a*	*b*
A_1	**4.56 ± 1.30**	0.07 ± 0.24	**3.61 ± 1.38**	**0.71 ± 0.25**
ϕ_1	9.85 ± 22.27	**4.52 ± 4.12**	**56.41 ± 13.42**	2.22 ± 2.44

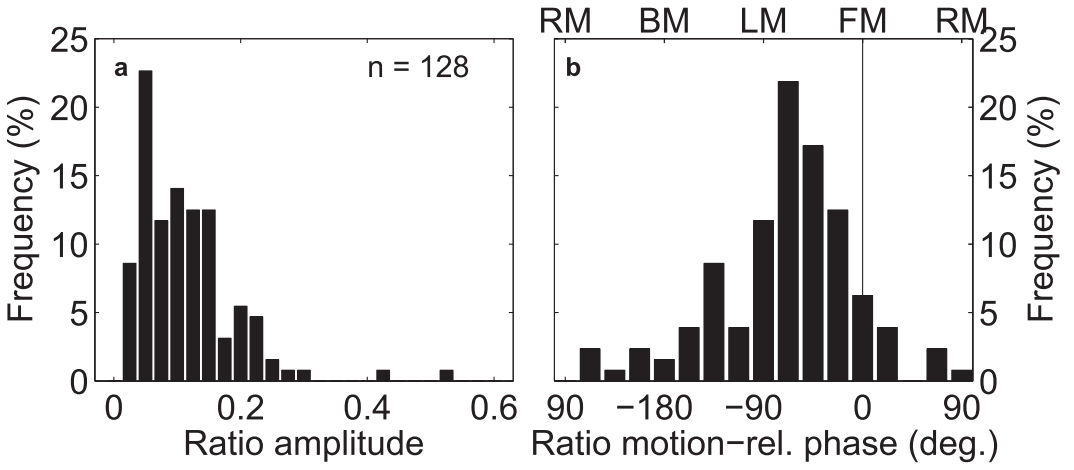

FIG. 9. Surface-to-flight-level wind speed ratio WN1 asymmetry (a) amplitude and (b) phase frequency histograms. Amplitude is dimensionless, and phase is in degrees azimuth clockwise relative to storm motion.

there appears to be no significant amplification of the surface-to-flight-level ratio asymmetry; however, there is a significant rotation of the asymmetry with increased shear. Over the range of observed shear from 0 to 15 m s^{-1}, the ratio asymmetry phase rotates from the DS direction to around 100° left of shear.

d. Asymmetry relationship to shear-relative motion

Although the estimated impact of storm motion on wind speed asymmetries was removed prior to examining the relationship of asymmetries to shear, it is not yet clear that the observed left-of-shear asymmetry generally

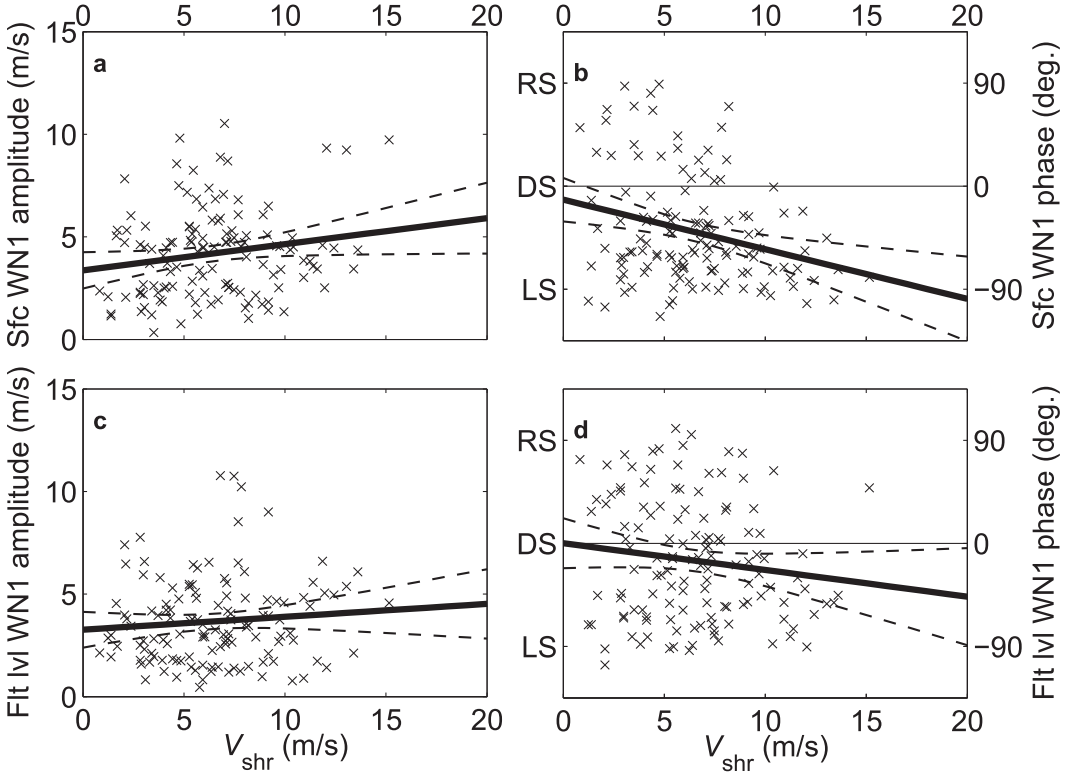

FIG. 10. As in Fig. 8, but plotted vs shear magnitude (m s^{-1}) after removing storm-motion-induced asymmetry. Phase angle (°) is clockwise azimuth relative to shear direction.

TABLE 3. As in Table 2, but for asymmetry vs shear magnitude after removing motion dependencies. Phase angles are clockwise relative to shear direction.

	Surface		Flight level	
	a	*b*	*a*	*b*
A_1	**3.37 ± 0.89**	0.13 ± 0.13	**3.26 ± 0.87**	0.06 ± 0.12
ϕ_1	−11.78 ± 19.08	**−4.34 ± 2.68**	0.15 ± 21.85	−2.33 ± 3.07

holds over all motion versus shear configurations. The relative impacts of motion and shear on convective asymmetries have previously been examined, with evidence pointing to a shear dominance (Corbosiero and Molinari 2003). Referring back to Fig. 3, there is a systematic relationship between motion and shear directions in the sample examined, as typically the shear heading is directed across the storm motion from left to right. This is consistent with a NW-traveling hurricane encountering an environmental shear from the SW. Under this configuration, a storm's right-front quadrant relative to motion is also the downshear-left quadrant relative to shear direction. Thus, the surface wind maxima relative to both motion and shear directions may be found at similar locations, on average.

To demonstrate that the left-of-shear wind maximum is a general result, the sample is stratified according to shear-relative motion ($\Delta\theta = \theta_{\text{storm}} - \theta_{\text{shr}}$), whose sample distribution was previously shown in Fig. 3c, depending on whether motion is downshear (DSHR), right of shear (RSHR), upshear (USHR), or left of shear (LSHR). The DSHR group ($n = 36$) contains storms traveling $-45° < \Delta\theta < +45°$, the RSHR group ($n = 36$) contains storms traveling $+45° < \Delta\theta < +135°$, the USHR group ($n = 27$) contains storms traveling $\Delta\theta < -135°$ or $> +135°$, and the LSHR group ($n = 39$) contains storms traveling $-135° < \Delta\theta < -45°$.

The mean characteristics of each subsample group are presented in Fig. 12. Note that mean motion and shear values are computed as vector averages, while mean direction differences are scalar averages. Generally, the DSHR group of storms is the most strongly sheared and has the most northward motion component, while the RSHR group is most weakly sheared and has the most westward motion component. The differences in motion speed among all groups are not statistically significant, while shear magnitude differences are marginally significant between the DSHR and RSHR groups. Shear-relative motion direction is controlled far more by the shear than the motion.

Figure 13 shows frequency histograms of the surface wind speed asymmetry WN1 amplitude and phase for each of the four shear-relative motion groups. Differences in amplitude and phase among each of the groups are not statistically significant. In all cases, the average residual asymmetry maximum is found in a downshear-left location. The asymmetric distribution of the surface-to-flight-level wind speed ratio is shown in Fig. 14 for each individual shear-relative motion group. The ratio asymmetry generally reflects the surface wind speed asymmetry, indicating that the largest ratios (after removing the motion dependence) are typically found in the DS to LS directions, in all cases. With the smaller sample sizes after stratifying according to shear-relative motion, quantifying asymmetry dependence on shear magnitude individually for each group remains difficult. However, it is clear that the environmental flow field (as represented here by the vertical shear) through which a storm moves may impact the surface wind asymmetry and, therefore, the asymmetric relationship between winds measured at the surface and well above the TC boundary layer.

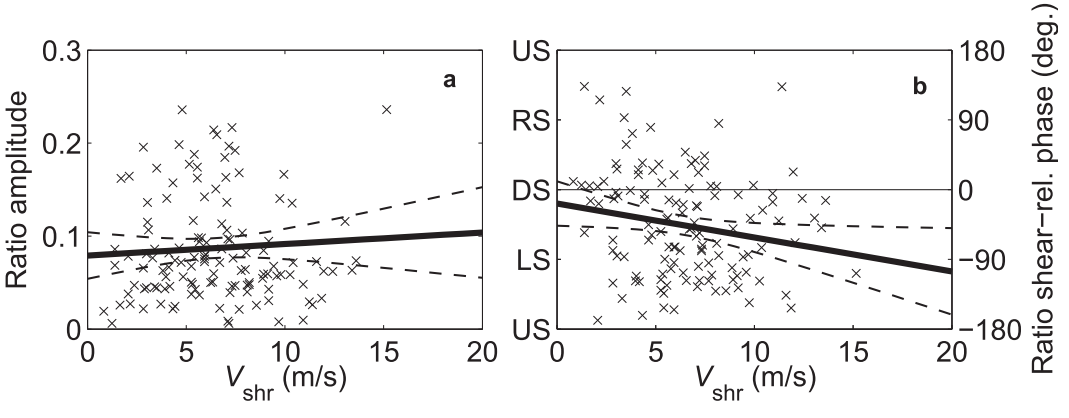

FIG. 11. Surface-to-flight-level wind speed ratio WN1 (a) asymmetry amplitude and (b) phase as a function of shear magnitude V_{shr} (m s^{-1}). Linear regression fits and 95% confidence intervals are also shown. Amplitude is dimensionless, and phase angle is azimuth relative to shear direction, with positive angles to the right of shear.

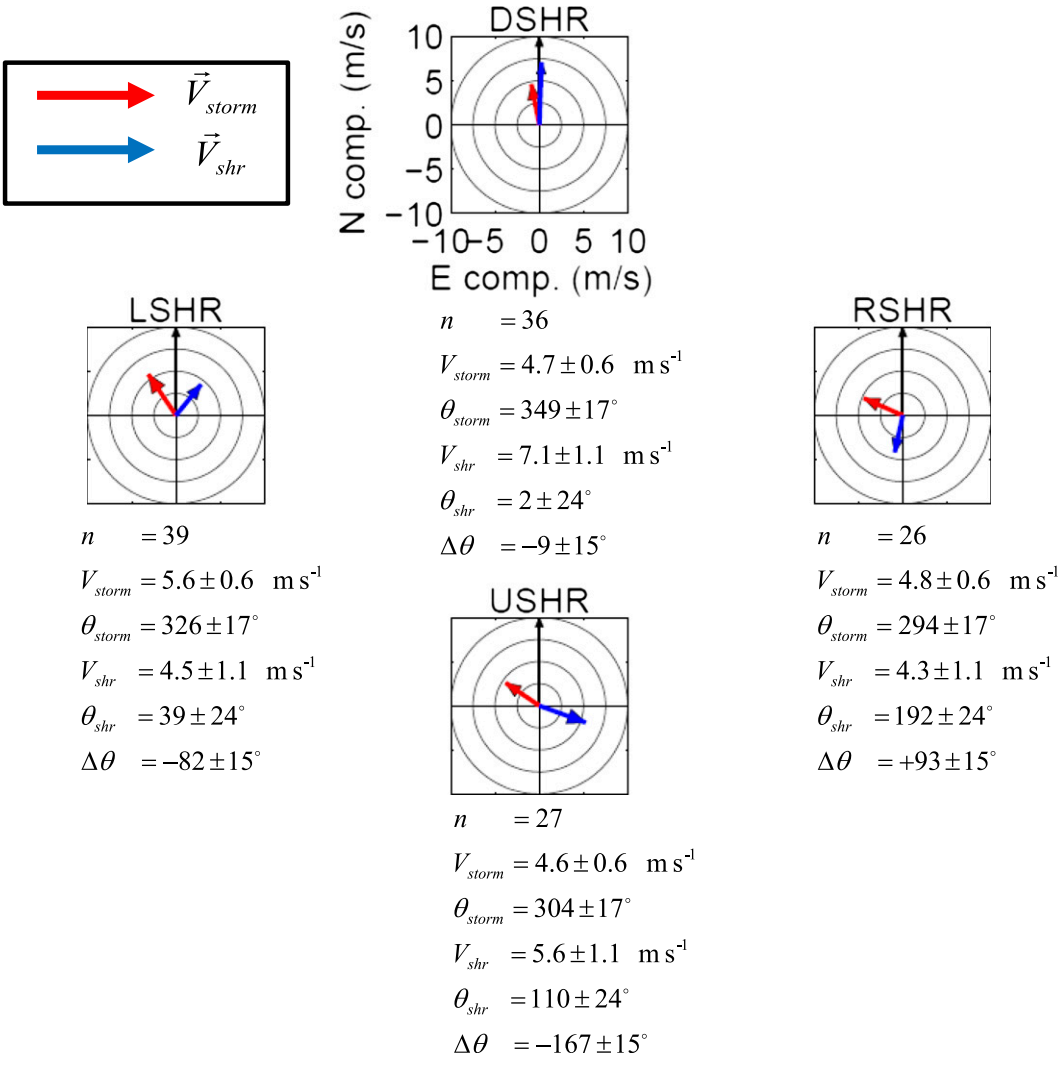

FIG. 12. Geographic orientation of mean shear and motion vectors for each shear-relative motion group. Polar plots show storm-motion vectors (red) and shear vectors (blue) in m s^{-1}, with radial rings at 2.5 m s^{-1} intervals. Black arrow points north. For each group, sample size (n), mean storm motion vector (V_{storm}, θ_{storm}), shear vector (V_{shr}, θ_{shr}), and vector direction difference ($\Delta\theta$) are labeled below each plot.

4. Case study: Hurricane Earl

a. General evolution

The wind field response to an evolving environmental shear is examined based on extensive aircraft observations obtained during Hurricane Earl (2010) throughout much of its life cycle. In particular, research aircraft missions were conducted roughly every 12 h over a 5-day period during rapid intensification, eyewall replacement, reintensification, and decay toward an extratropical cyclone. Additionally, several operational reconnaissance flights were executed. In all, a total of 18 SFMR surface and flight-level wind analyses were constructed between 29 August and 4 September 2010 while Earl was classified as a hurricane.

Earl's track over the period of interest is shown in Fig. 15, and time series of best track intensity, SFMR-observed surface RMW, storm motion, and shear vectors are shown in Fig. 16. The storm motion speed was a fairly steady ~5–7 m s^{-1} over most of the period, as Earl progressed on a gradual recurvature, from a westward to a northward heading. Over this period, the storm rapidly intensified between 29 and 30 August, reaching an initial peak intensity of nearly 60 m s^{-1} (115 kt, 1 kt = 0.51 m s^{-1}), while the RMW contracted from >50 to ~20 km (Fig. 16a). On 31 August, Earl

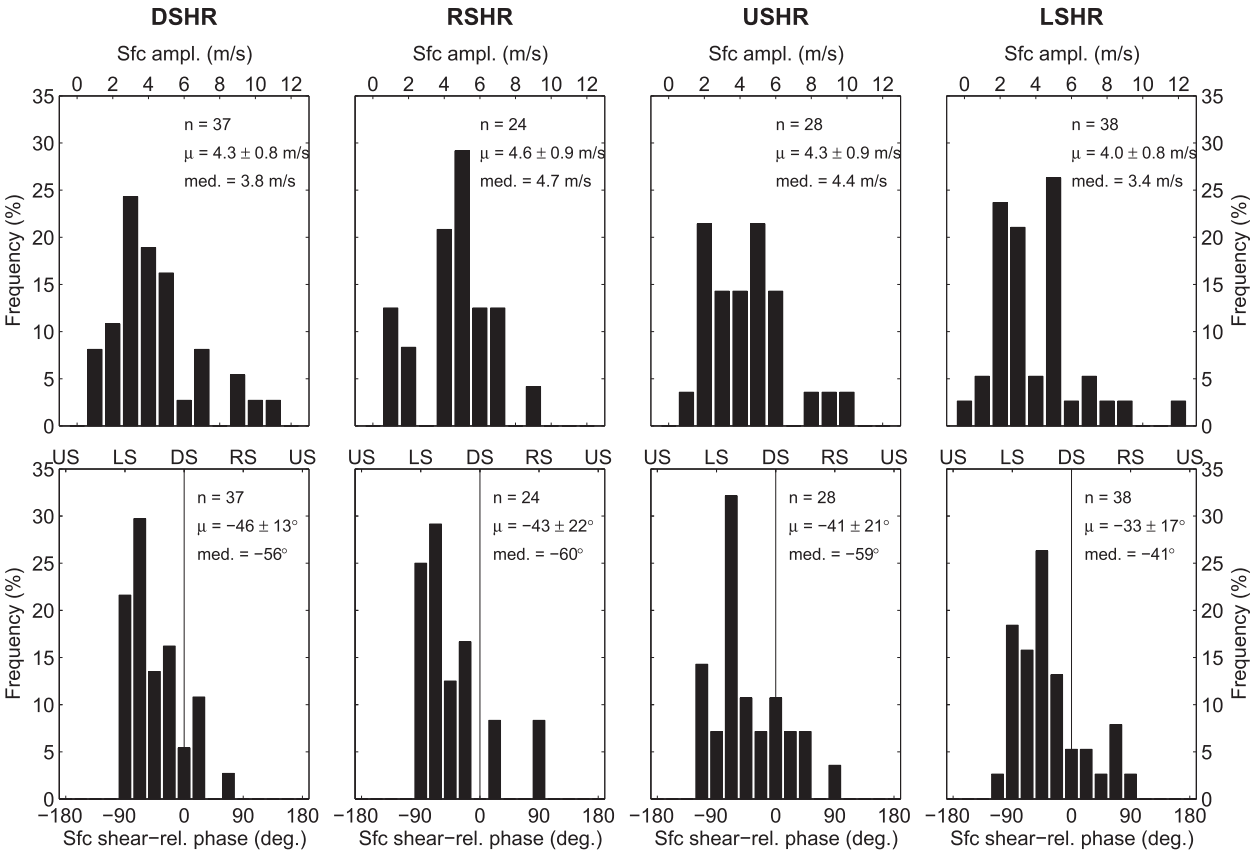

FIG. 13. Frequency distributions of surface WN1 asymmetry (top) amplitude and (bottom) phase for each shear-relative motion group. Columns are (left) DSHR, (middle left) RSHR, (middle right) USHR, and (right) LSHR. Sample sizes, means with 95% confidence intervals, and medians are indicated.

began an eyewall-replacement cycle, with a slight weakening and increase in the RMW. The storm re-intensified to its maximum intensity of 64 m s^{-1} (125 kt) on 2 September, before beginning a gradual weakening and wind field expansion.

Early in the period, the shear was weak and from the NE, when Earl rapidly intensified. The shear magnitude increased subsequent to the initial intensification (Fig. 16b), while the direction rotated through easterly to become southerly when eyewall replacement began (Fig. 16c). After this, the shear magnitude weakened slightly, and the direction remained relatively constant for the remainder of the observation period to 4 September. The shear-relative motion direction ($\Delta\theta$) executed nearly a continuous full cycle, rotating at an average rate of ~60° day^{-1} over this 6-day period (Fig. 16d).

Surface and flight-level wind field evolutions derived from the Fourier analyses are shown in Fig. 17 for each of 5 days (30 August–3 September) at 0000 UTC. Fields are plotted relative to storm motion direction, as indicated by black arrows. The motion-relative shear vectors are also plotted as white arrows. Beginning on 30 August, a fairly weak shear is directed across the storm track from right to left, and becomes stronger and rotates counterclockwise to align closely with the storm motion direction by the end of the period. The flight-level asymmetry is mostly located to the right of track, with a weak counterclockwise rotation in time. The surface wind maximum (indicated by the plus sign) begins on 30 August to the right of track when the shear is weaker, and rotates counterclockwise in time to the front of the storm by 3 September. When the shear is sufficiently strong from 31 August on, the surface asymmetry maximum maintains a downshear to downshear-left location, deviating from the expected motion-induced asymmetry. The flight-level peak remains more closely locked to the motion, although some small variation is observed. A similar evolution was noted in Hurricane Rita over a 3-day period (Rogers and Uhlhorn 2008), in which the shear steadily increased and rotated counterclockwise in time, while the surface wind asymmetry changed from right of storm motion to being in front of the storm.

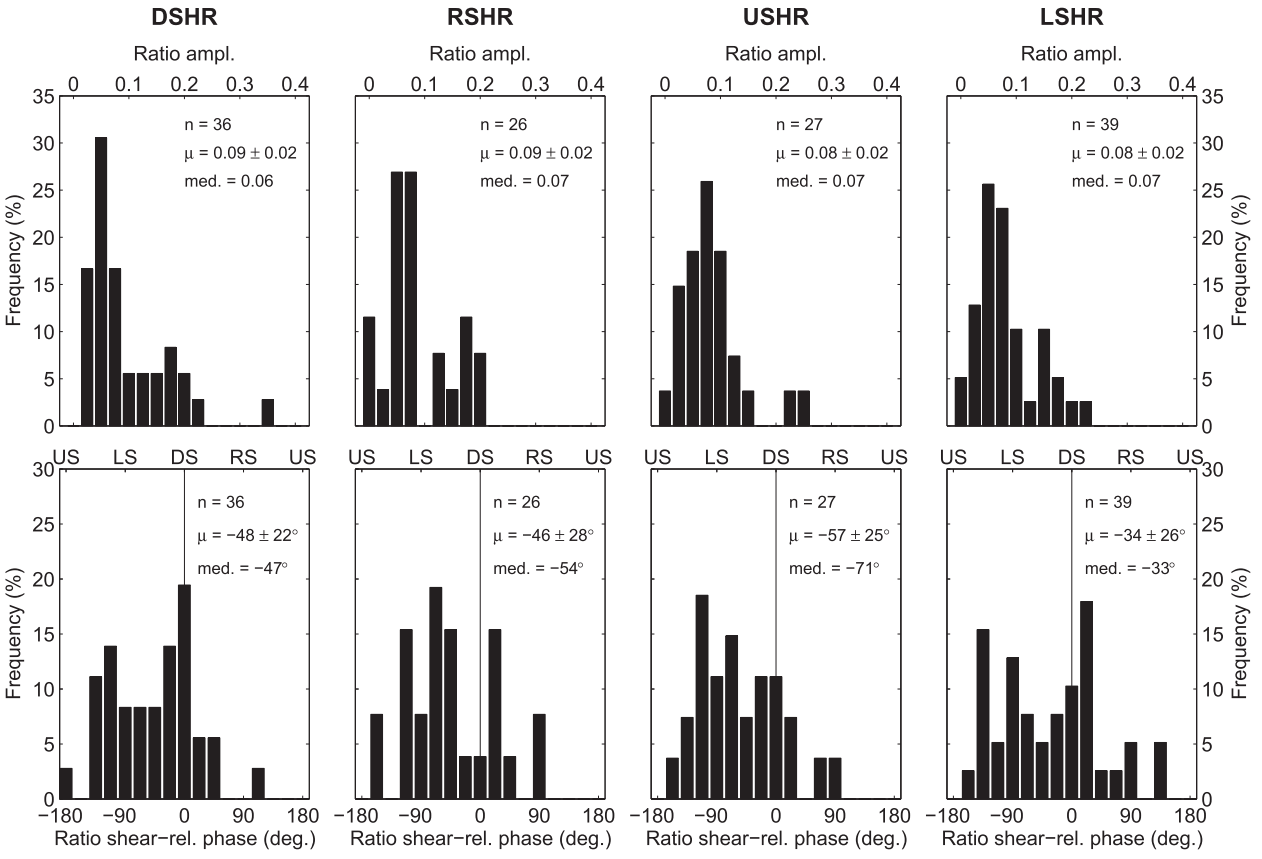

FIG. 14. As in Fig. 13, but for surface-to-flight-level ratio.

b. Asymmetry evolution

The WN0 + 1 analyses at the surface and flight level are interpolated in time every 12 h, beginning at 1200 UTC 29 August, through 1200 UTC 3 September. Figure 18 shows surface and flight-level WN0 means, and WN1 amplitudes and motion-relative phases as functions of radius and time over the observation period. The dual WN0 maxima at both surface and flight levels on 31 August and 2 September are clearly evident, along with the local intensity minimum associated with eyewall replacement on 1 September. Associated with the replacement is a large increase in asymmetry, particularly at the flight level. Also, a significant asymmetry at the surface appears at $r^* \sim 4$ late during the period on 3 September, suggesting a developing outer wind maximum. At the flight level, the asymmetry phase varies by no more than 30°, and is generally right of motion at all radii throughout. At the surface, however, the phase rotates counterclockwise in time by more than 60° at the RMW from right of motion to in front of the storm; these changes are even more evident at larger radii. Since these analyses are relative to storm motion direction, and storm motion speed only varies by around $2\,\mathrm{m\,s^{-1}}$ over this period, changes in asymmetry may be interpreted as a result of mechanisms other than storm motion.

The WN1 asymmetry amplitude at the RMW is shown in Fig. 19. The evolution (Fig. 19a) suggests an amplifying asymmetry from early in the period, to a peak

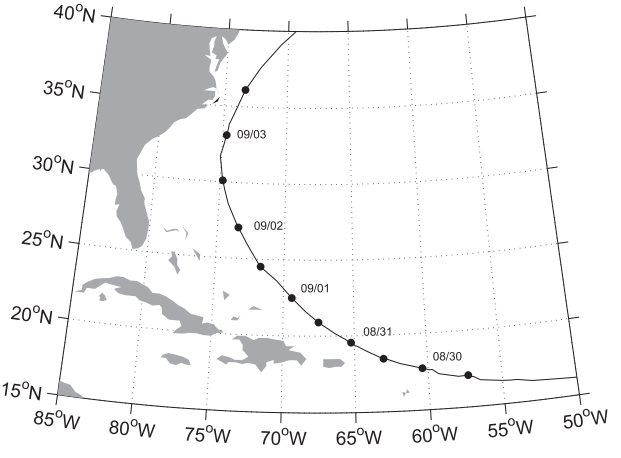

FIG. 15. Hurricane Earl (2010) track. Storm locations are marked at 12-h intervals, and labeled as month/day.

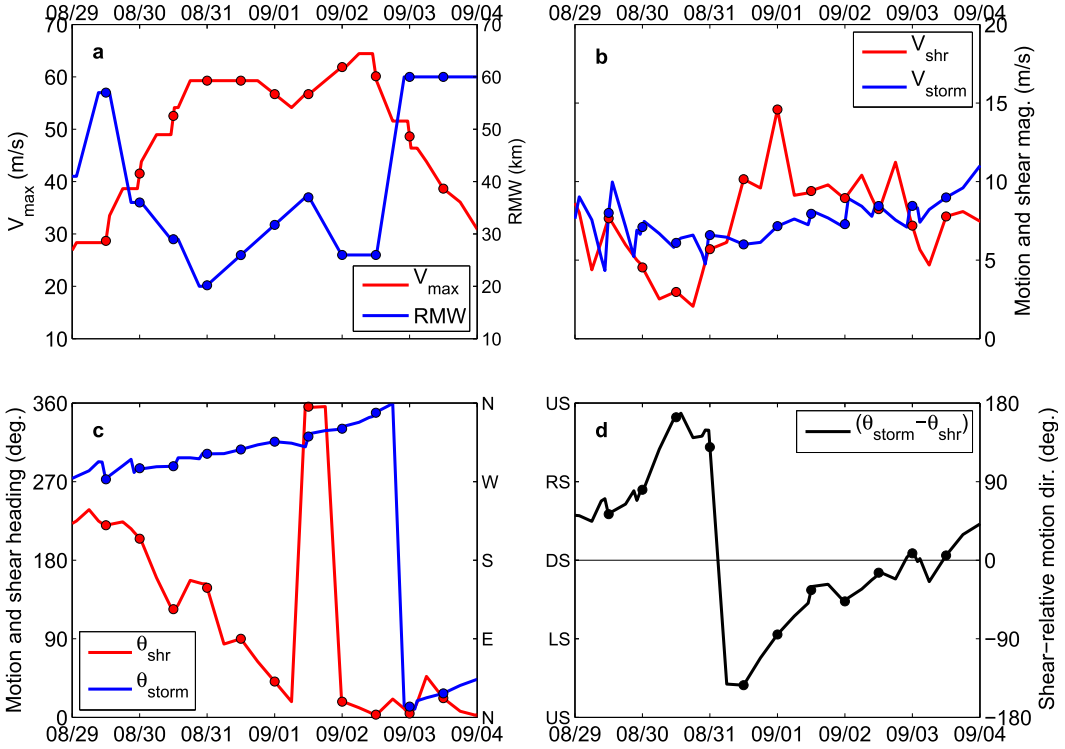

FIG. 16. Hurricane Earl time series of (a) intensity and RMW, (b) storm motion speed and shear magnitude, (c) storm motion and shear headings, and (d) shear-relative motion direction.

around the time of eyewall replacement, and then a gradual return to a more symmetric wind field later in time. At both the surface and flight level, there is little relationship between amplitude and V_{storm} (Fig. 19b), as linear trends are not significant, although the motion does not vary a great deal, as previously noted. In contrast, there is a strong relationship between the amplitude and V_{shr} (Fig. 19b) for this particular storm. Linear trends are significant at the 95% confidence level, and correlation coefficients are $r^2 = 0.61$ and 0.87 at the surface and flight levels, respectively.

The ratio of surface-to-flight-level wind speed WN1 asymmetry is tracked through Earl's life cycle. As the storm progressed, the location of the flight-level wind maximum remained to the right of motion, while the surface maximum rotated counterclockwise from right to forward of motion, maintaining a downshear-left position as the shear vector rotated with time. To emphasize the potential shear control on the asymmetry, the reduction ratio phases are computed relative to storm motion direction and plotted versus V_{storm} (Fig. 20a), and relative to shear direction plotted versus V_{shr} (Fig. 20b). Motion-relative phase is typically to the left of motion, as previously found by Powell et al. (2009), and shown in Fig. 9b. In Earl, however, there is no significant dependence on V_{storm}. In sharp contrast, the shear-relative reduction asymmetry phase has a strong dependence on V_{shr}, consistent with the results for the full sample (Fig. 11), suggesting the counterclockwise rotation from the DS position to LS, as the shear magnitude increases.

5. Discussion

A couple of recent studies have found evidence for an environmental shear impact on west Pacific typhoon near-surface wind WN1 asymmetries (Ueno and Kunii 2009; Ueno and Bessho 2011). In addition, Ueno and Kunii (2009) suggested a link between the eyewall vertical velocity asymmetry and the boundary layer tangential wind asymmetry. Overall, their results suggested a preferential downshear-left azimuthal location for the storm-relative maximum wind, and when the shear was strong and aligned with the motion, a left-of-motion *earth-relative* wind maximum could be found. In the present study, 28 out of the 128 (23%) total analyzed cases indicated a left-of-motion surface wind maximum (Fig. 8b). When broken down by shear-relative motion direction, 41% of the DSHR cases contained a left-of-motion maximum. In contrast, only 18% of both the RSHR and USHR cases showed the maximum located left of motion, and 11% of the LSHR cases contained

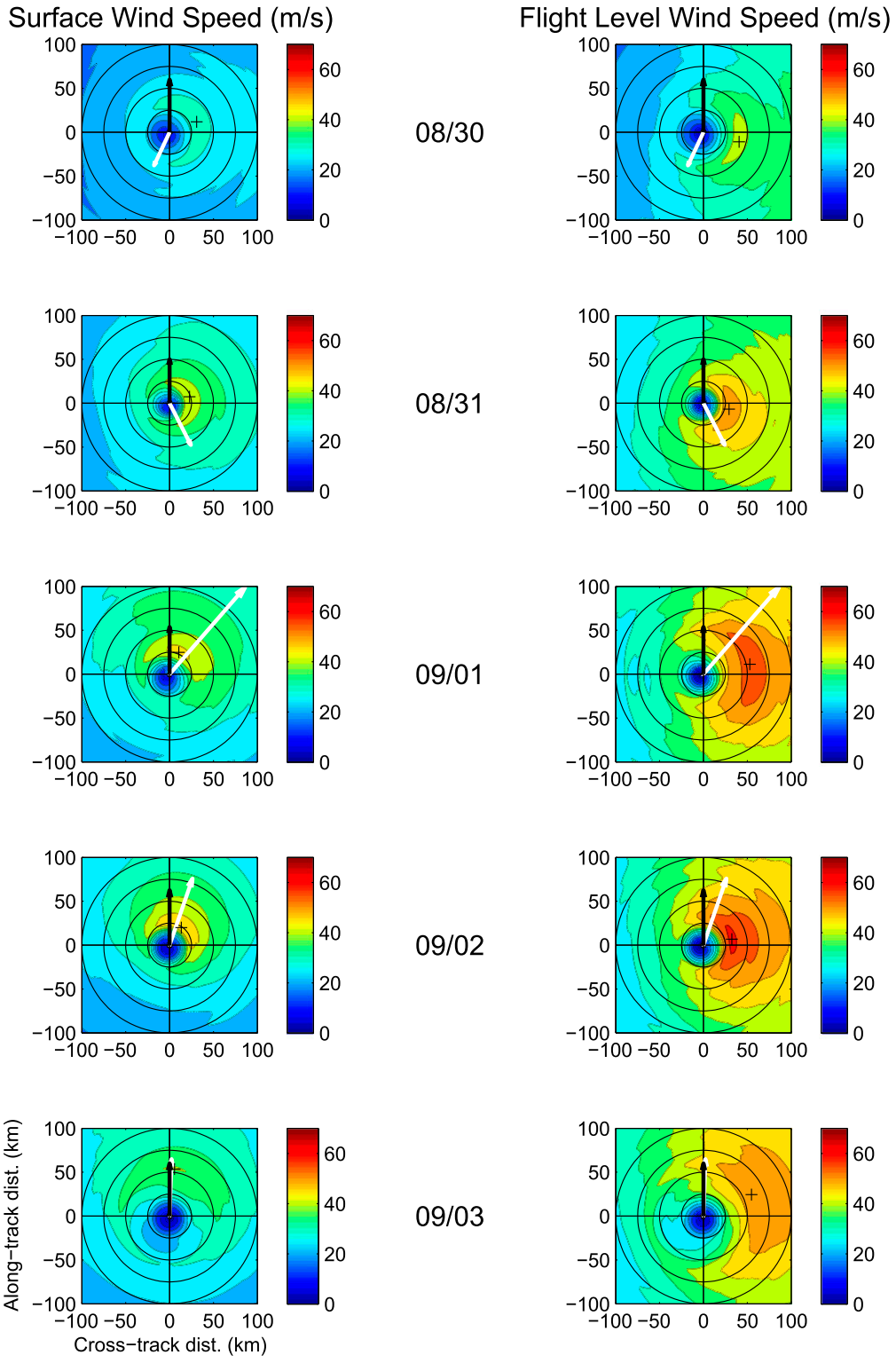

FIG. 17. Hurricane Earl wind speed ($m\,s^{-1}$) analyses at (left) the surface and (right) flight level, corresponding to 0000 UTC on date indicated (month/day). Analyses are oriented with respect to storm motion direction, with across- (along-) track distance (km) labeled along the x (y) axis. Black arrows show the storm motion vector, and white arrows the shear vector. Range rings indicate magnitude ($m\,s^{-1}$) at $2.5\,m\,s^{-1}$ intervals, or $^{1}/_{10}$ axis labels.

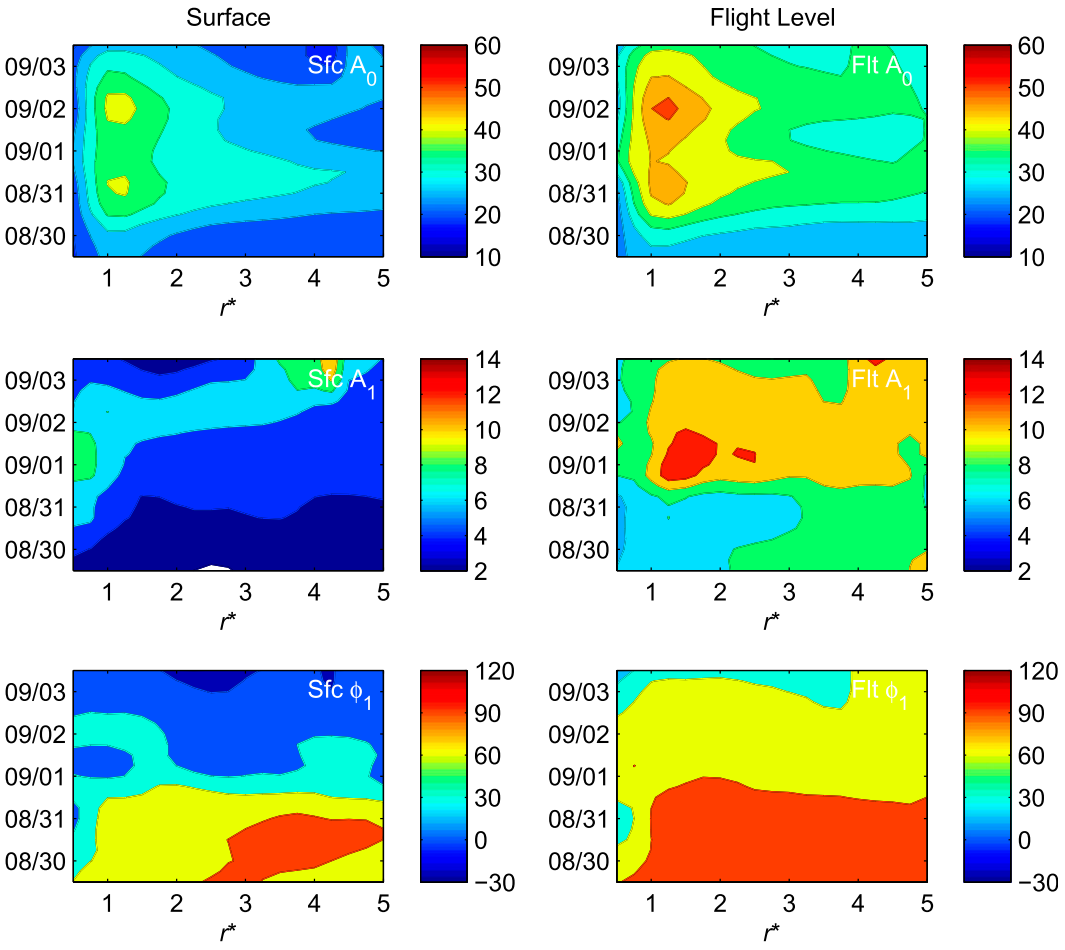

FIG. 18. Hurricane Earl (left) surface and (right) flight-level (top) WN0, (middle) WN1 amplitude, and (bottom) WN1 motion-relative phase Hovmöller plots. Mean (A_0) and amplitude (A_1) are in m s^{-1}, and phase (ϕ_1) is in degrees azimuth clockwise relative to storm motion direction.

a left-of-motion earth-relative wind speed maximum. Additionally, the DSHR, left-of-motion wind maximum group is also the most strongly sheared, on average. These results imply that the horizontal surface wind field in TCs influenced by shear may deviate systematically from the expected motion-induced asymmetric structure (Shapiro 1983; Kepert 2001; Kepert and Wang 2001). Parametric wind fields designed to accurately capture low-wavenumber asymmetry should consider the important shear impact.

Numerous observational studies have sought to relate environmental shear to convection asymmetries in TCs from airborne radar reflectivity (e.g., Reasor et al. 2000; Black et al. 2002; Reasor and Eastin 2012), spaceborne passive microwave measurements (e.g., Knaff et al. 2004; Chen et al. 2006; Cecil 2007; Wingo and Cecil 2010), and lightning distribution (Corbosiero and Molinari 2002, 2003), with the common conclusion that an inner-core precipitation maximum is typically found in a downshear-left location. Additionally, observations of airborne Doppler radar–derived vertical velocity (e.g., Black et al. 2002; Reasor et al. 2009, 2013) indicate the main updraft maximum is typically located downshear and in the direction of eyewall tilt. Modeling studies have shown the maximum storm-relative low-level radial inflow to also be located generally downshear (Bender 1997; Rogers et al. 2003; Wu et al. 2006; Braun and Wu 2007; Davis et al. 2008).

From a storm-relative vantage point, the tangential and radial wind component asymmetries are in quadrature (Schwendike and Kepert 2008; Ueno and Bessho 2011), with the tangential wind maximum $\pi/2$ rad clockwise from the radial wind maximum. From continuity, the low-level radial flow and vertical velocity asymmetries are π rad out of phase (i.e., the radial flow maximum is upshear). When the environmental shear is sufficient, the main updraft maximum becomes more isolated in the downshear position, and from this analysis, the tangential wind maximum is therefore located left of

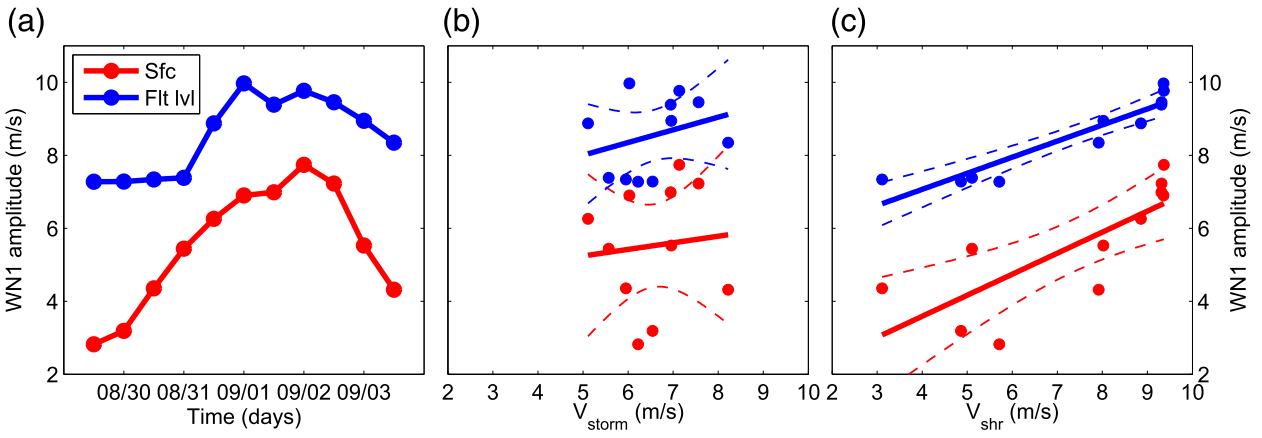

FIG. 19. (a) Time series of analyzed WN1 asymmetry amplitude for Hurricane Earl at surface (red) and flight level (blue) every 12 h, (b) WN1 ampliude vs V_{storm} ($m\,s^{-1}$), and (c) WN1 amplitude vs V_{shear} ($m\,s^{-1}$).

shear. It can be easily shown that the *wind speed* WN1 asymmetry phase (ϕ_{s1}) is related to the radial component asymmetry by

$$\phi_{s1} = \cos^{-1}\left(\frac{A_{u0}A_{u1}}{A_{s0}A_{s1}}\right), \qquad (2)$$

where A_{u0}, A_{u1} are the axisymmetric mean and WN1 amplitudes of radial wind, respectively. Based on results in this study along with recent observations of TC inflow asymmetries derived from dropwindsondes, the expected wind speed asymmetry phase may be estimated.

As found by Zhang and Uhlhorn (2012), the axisymmetric mean storm-relative inflow angle at the RMW is $-20.2° \pm 2.2°$ (95% confidence) for a typical hurricane, which results in $A_{u0}/A_{s0} \approx -0.34$. Also, the storm-relative inflow angle WN1 amplitude at the RMW was found to be $9.2° \pm 2.0°$. For a mean wind speed of $A_{s0} = 40\,m\,s^{-1}$, the radial wind asymmetry amplitude is $A_{u1} \approx 7.4\,m\,s^{-1}$ (Zhang and Uhlhorn, 2012). Results from the present study indicate $A_{s1} \approx 4.1\,m\,s^{-1}$ (see Fig. 13), suggesting the ratio $A_{u1}/A_{s1} \approx 1.8$. Substituting these values into Eq. (2) results in an expected near-surface wind WN1 asymmetry phase relative to the radial flow maximum of $\phi_{s1} \approx +128°$, or $-52°$ relative to the inflow maximum. Assuming the inflow and shear directions are collocated, this places the wind speed maximum in the downshear-left quadrant, in agreement with the observations here. Based on this simple interpretation, the convective and near-surface kinematic asymmetries appear to be interrelated in a highly systematic way, which the vertical shear exposes when sufficiently strong.

6. Summary and conclusions

Based on an analysis of SFMR surface and in situ flight-level wind data obtained on 128 hurricane aircraft

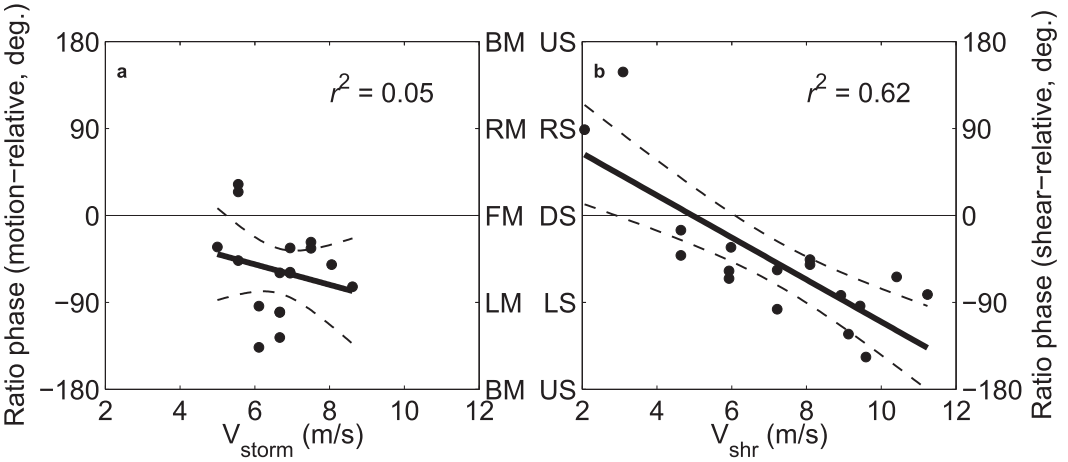

FIG. 20. Surface-to-flight-level wind speed ratio WN1 asymmetry phase (°) for Hurricane Earl analyses, relative to (a) storm-motion direction and as a function of V_{storm} and (b) shear direction and as a function of V_{shr}.

missions, the asymmetric wind structure at the RMW in response to motion and 850–200-mb environmental shear is documented. The analysis consists of an azimuthal WN0 + 1 Fourier decomposition from high radial resolution wind speed observations, designed to yield the WN0 symmetric mean, and WN1 amplitude and phase, as functions of radial distance from the storm center. The important findings of this study are as follows:

- Storm motion impacts flight-level and surface wind asymmetries differently. At flight level, amplitude increases in proportion to motion speed, while phase is locked nearly directly to the right of motion direction, independent of speed. At the surface, amplitude is nearly constant, while phase rotates from front to right of motion direction as speed increases.
- Relative to storm motion direction, the asymmetry amplitude of the surface-to-flight-level wind speed (slant) ratio at the RMW is broadly distributed with a median value around 0.1 (i.e., the ratio typically varies by ~20% around the eyewall), while the maximum location is found to the left of the motion. No ratio asymmetry dependence on motion is found.
- After accounting for, and removing, the motion dependence, a residual asymmetry component relative to the shear direction is found, especially at the surface. A significant phase rotation from downshear to left of shear with increased shear magnitude is observed, regardless of the relationship between motion and shear directions. The flight-level phase response is comparatively weaker.
- The evolution of wind asymmetries in Hurricane Earl (2010) over a 5-day period clearly shows the response of the total, motion plus shear, impact. The flight-level wind maximum generally remains to the right of the storm track over the period while the shear increases. The surface wind maximum begins right of track early in the period and, as shear increases, rotates counterclockwise, remaining to the left of shear direction. As a result of this gradual phase separation, the surface-to-flight-level wind speed ratio maximum at the RMW has little relationship with storm motion speed (r^2 = 0.05), and a strong relationship with shear magnitude (r^2 = 0.62).

These results appear to support recent conclusions about shear impacts on typhoon asymmetries, which find that a left-of-shear direction storm-relative wind maximum is to be expected. When the shear is sufficiently strong and roughly aligned with the motion direction, the motion and shear-induced asymmetries can combine to yield a left-of-motion earth-relative wind maximum location. The results of this study are generally supportive of these findings.

Because the SFMR only measures the wind speed, observations of near-surface radial and tangential wind asymmetries, and their relationships to vertical wind and convection asymmetric structure, have not been directly analyzed in this study. A more complete observational view of the surface to upper-tropospheric kinematics in sheared environments remains to be developed. Planned future efforts will involve combining the results found here with composite analyses of surface wind vector field asymmetries using GPS dropwindsonde data, and linking the results to Doppler radar–derived wind and thermodynamic fields.

Acknowledgments. The authors would like to acknowledge John Kaplan, Drs. Sundararaman Gopalakrishnan, and Mark Powell (HRD), as well as two anonymous reviewers, for their comments and suggestions that significantly improved the manuscript. B. Klotz is partially supported through the Joint Hurricane Testbed and Hurricane Forecast Improvement Project.

REFERENCES

Aksoy, A., S. D. Aberson, T. Vukicevic, K. J. Sellwood, S. Lorsolo, and X. Zhang, 2013: Assimilation of high-resolution tropical cyclone observations with an ensemble Kalman filter using NOAA/AOML/HRD's HEDAS: Evaluation of the 2008-11 vortex-scale analyses. *Mon. Wea. Rev.,* **141,** 1842–1865.

Barnes, S., 1964: A technique for maximizing details in numerical weather map analysis. *J. Appl. Meteor.,* **3,** 396–409.

Bell, M. M., M. T. Montgomery, and K. A. Emanuel, 2012: Air–sea enthalpy and momentum exchange at major hurricane wind speeds observed during CBLAST. *J. Atmos. Sci.,* **69,** 3197–3222.

Bender, M. A., 1997: The effect of relative flow on the asymmetric structure in the interior of hurricanes. *J. Atmos. Sci.,* **54,** 703–724.

Bergman, K. H., 1979: Multivariate analyses of temperatures and winds using optimum interpolation. *Mon. Wea. Rev.,* **107,** 1423–1444.

Black, M. L., J. F. Gamache, F. D. Marks Jr., C. E. Samsury, and H. E. Willoughby, 2002: Eastern Pacific Hurricanes Jimena of 1991 and Olivia of 1994: The effect of vertical shear on structure and intensity. *Mon. Wea. Rev.,* **130,** 2291–2312.

Braun, S. A., and L. Wu, 2007: A numerical study of Hurricane Erin (2001). Part II: Shear and the organization of eyewall vertical motion. *Mon. Wea. Rev.,* **135,** 1179–1194.

——, and Coauthors, 2013: NASA's Genesis and Rapid Intensification Processes (GRIP) field experiment. *Bull. Amer. Meteor. Soc.,* **94,** 345–363.

Cecil, D. J., 2007: Satellite-derived rain rates in vertically sheared tropical cyclones. *Geophys. Res. Lett.,* **34,** L02811, doi:10.1029/2006GL027942.

Chen, S., J. A. Knaff, and F. D. Marks, 2006: Effects of vertical wind shear and storm motion on tropical cyclone rainfall asymmetries deduced from TRMM. *Mon. Wea. Rev.,* **134,** 3190–3208.

Corbosiero, K. L., and J. Molinari, 2002: The effects of vertical wind shear on the distribution of convection in tropical cyclones. *Mon. Wea. Rev.,* **130,** 2110–2123.

——, and ——, 2003: The relationship between storm motion, vertical wind shear, and convective asymmetries in tropical cyclones. *J. Atmos. Sci.,* **60,** 366–376.

Davis, C., and Coauthors, 2008: Prediction of landfalling hurricanes with the Advanced Hurricane WRF model. *Mon. Wea. Rev.,* **136,** 1990–2005.

DeMaria, M., M. Mainelli, L. K. Shay, J. A. Knaff, and J. Kaplan, 2005: Further improvements to the Statistical Hurricane Intensity Prediction Scheme (SHIPS). *Wea. Forecasting,* **20,** 531–543.

Didlake, A. C., Jr., and R. A. Houze Jr., 2009: Convective-scale downdrafts in the principal rainband of Hurricane Katrina (2005). *Mon. Wea. Rev.,* **137,** 3269–3293.

Frank, W. M., and E. A. Ritchie, 2001: Effects of vertical wind shear on the intensity and structure of numerically simulated hurricanes. *Mon. Wea. Rev.,* **129,** 2249–2269.

Franklin, J. L., M. L. Black, and K. Valde, 2003: GPS dropwindsonde wind profiles in hurricanes and their operational implications. *Wea. Forecasting,* **18,** 32–44.

Georgiou, P., 1985: Design wind speeds in tropical cyclone prone regions. Ph.D. thesis, University of Western Ontario, 295 pp.

Hence, D. A., and R. A. Houze Jr., 2008: Kinematic structure of convective-scale elements in the rainbands of Hurricanes Katrina and Rita (2005). *J. Geophys. Res.,* **113,** D15108, doi:10.1029/2007JD009429.

Holland, G. J., 1980: An analytic model of the wind and pressure profiles in hurricanes. *Mon. Wea. Rev.,* **108,** 1212–1218.

——, J. I. Belanger, and A. Fritz, 2010: A revised model for radial profiles of hurricane winds. *Mon. Wea. Rev.,* **138,** 4393–4401.

Houston, S. H., W. A. Shaffer, M. D. Powell, and J. Chen, 1999: Comparisons of HRD and SLOSH surface wind fields in hurricanes: Implications for storm surge modeling. *Wea. Forecasting,* **14,** 671–686.

Hu, K., Q. Chen, and S. K. Kimball, 2012: Consistency in hurricane surface wind forecasting: An improved parametric model. *Nat. Hazards,* **61,** 1029–1050.

Irish, J. L., D. T. Resio, and J. J. Ratcliff, 2008: The influence of storm size on hurricane surge. *J. Phys. Oceanogr.,* **38,** 2003–2013.

Jarvinen, B. R., C. J. Neumann, and M. A. S. Davis, 1984: A tropical cyclone data tape for the North Atlantic Basin, 1886–1983: Contents, limitations, and uses. NOAA Tech. Memo. 22, NWS/NHC, Miami, FL, 21 pp.

Kepert, J., 2001: The dynamics of boundary layer jets within the tropical cyclone core. Part I: Linear theory. *J. Atmos. Sci.,* **58,** 2469–2484.

——, 2006a: Observed boundary layer wind structure and balance in the hurricane core. Part I: Hurricane Georges. *J. Atmos. Sci.,* **63,** 2169–2193.

——, 2006b: Observed boundary layer wind structure and balance in the hurricane core. Part II: Hurricane Mitch. *J. Atmos. Sci.,* **63,** 2194–2211.

——, and Y. Wang, 2001: The dynamics of boundary layer jets within the tropical cyclone core. Part II: Nonlinear enhancement. *J. Atmos. Sci.,* **58,** 2485–2501.

Knaff, J. A., and R. M. Zehr, 2007: Reexamination of tropical cyclone wind–pressure relationships. *Wea. Forecasting,* **22,** 71–88.

——, J. P. Kossin, and M. DeMaria, 2003: Annular hurricanes. *Wea. Forecasting,* **18,** 204–223.

——, S. Seseske, M. DeMaria, and J. Demuth, 2004: On the influences of vertical wind shear on symmetric tropical cyclone structure derived from AMSU. *Mon. Wea. Rev.,* **132,** 2503–2510.

——, M. DeMaria, D. A. Molenar, C. R. Sampson, and M. G. Seybold, 2011: An automated, objective, multiple-satellite platform tropical cyclone surface wind analysis. *J. Appl. Meteor. Climatol.,* **50,** 2149–2166.

Kossin, J. P., and W. H. Schubert, 2001: Mesovortices, polygonal flow patterns, and rapid pressure falls in hurricane-like vortices. *J. Atmos. Sci.,* **58,** 2196–2209.

Landsea, C. W., and Coauthors, 2004: A reanalysis of Hurricane Andrew's intensity. *Bull. Amer. Meteor. Soc.,* **85,** 1699–1712.

Mallen, K. J., M. T. Montgomery, and B. Wang, 2005: Reexamining the near-core radial structure of the tropical cyclone primary circulation: Implications for vortex resiliency. *J. Atmos. Sci.,* **62,** 408–425.

Marks, F. D., P. G. Black, M. T. Montgomery, and R. W. Burpee, 2008: Structure of the eye and eyewall of Hurricane Hugo (1989). *Mon. Wea. Rev.,* **136,** 1237–1259.

Nolan, D. S., J. A. Zhang, and D. P. Stern, 2009: Evaluation of planetary boundary layer parameterizations in tropical cyclones by comparison of in situ observations and high-resolution simulations of Hurricane Isabel (2003). Part I: Initialization, maximum winds, and the outer-core boundary layer. *Mon. Wea. Rev.,* **137,** 3651–3674.

Powell, M. D., and S. H. Houston, 1996: Hurricane Andrew's landfall in south Florida. Part I: Surface wind fields and potential real-time applications. *Wea. Forecasting,* **11,** 329–349.

——, and T. A. Reinhold, 2007: Tropical cyclone destructive potential by integrated kinetic energy. *Bull. Amer. Meteor. Soc.,* **88,** 513–526.

——, P. P. Dodge, and M. L. Black, 1991: The landfall of Hurricane Hugo in the Carolinas: Surface wind distribution. *Wea. Forecasting,* **6,** 379–399.

——, P. J. Vickery, and T. A. Reinhold, 2003: Reduced drag coefficient for high wind speeds in tropical cyclones. *Nature,* **422,** 279–283.

——, E. W. Uhlhorn, and J. D. Kepert, 2009: Estimating maximum surface winds from hurricane reconnaissance measurements. *Wea. Forecasting,* **24,** 868–883.

——, and Coauthors, 2010: Reconstruction of Hurricane Katrina's wind fields for storm surge and wave hindcasting. *Ocean Eng.,* **37,** 26–36.

Reasor, P. D., and M. Eastin, 2012: Rapidly intensifying Hurricane Guillermo (1997). Part II: Resilience in shear. *Mon. Wea. Rev.,* **140,** 425–444.

——, M. T. Montgomery, F. D. Marks Jr., and J. F. Gamache, 2000: Low-wavenumber structure and evolution of the hurricane inner core observed by airborne dual-Doppler radar. *Mon. Wea. Rev.,* **128,** 1653–1680.

——, ——, and L. D. Grasso, 2004: A new look at the problem of tropical cyclones in vertical shear flow: Vortex resiliency. *J. Atmos. Sci.,* **61,** 3–22.

——, M. Eastin, and J. F. Gamache, 2009: Rapidly intensifying Hurricane Guillermo (1997). Part I: Low-wavenumber structure and evolution. *Mon. Wea. Rev.,* **137,** 603–631.

——, R. F. Rogers, and S. Lorsolo, 2013: Environmental flow impacts on tropical cyclone structure diagnosed from airborne Doppler radar composites. *Mon. Wea. Rev.,* **141,** 2949–2969.

Riemer, M., M. T. Montgomery, and M. E. Nicholls, 2010: A new paradigm for intensity modification of tropical cyclones: Thermodynamic impact of vertical wind shear on the inflow layer. *Atmos. Chem. Phys.,* **10,** 3163–3188.

Rogers, R., and E. Uhlhorn, 2008: Observations of the structure and evolution of surface and flight-level wind asymmetries in Hurricane Rita (2005). *Geophys. Res. Lett.,* **35,** L22811, doi:10.1029/2008GL034774.

——, S. Chen, J. Tenerelli, and H. Willoughby, 2003: A numerical study of the impact of vertical shear on the distribution of rainfall in Hurricane Bonnie (1998). *Mon. Wea. Rev.,* **131,** 1577–1599.

Ross, R. J., and Y. Kurihara, 1992: A simplified scheme to simulate asymmetries due to the beta effect in barotropic vortices. *J. Atmos. Sci.,* **49,** 1620–1628.

Schwendike, J., and J. D. Kepert, 2008: The boundary layer winds in Hurricanes Danielle (1998) and Isabel (2003). *Mon. Wea. Rev.,* **136,** 3168–3192.

Shapiro, L. J., 1983: The asymmetric boundary layer flow under a translating hurricane. *J. Atmos. Sci.,* **40,** 1984–1998.

Sheets, R. C., 2003: Hurricane surveillance by specially instrumented aircraft. *Hurricane! Coping with Disaster,* R. Simpson, Ed., Amer. Geophys. Union, 63–101.

Stern, D. P., and D. S. Nolan, 2009: Reexamining the vertical structure of tangential winds in tropical cyclones: Observations and theory. *J. Atmos. Sci.,* **66,** 3579–3600.

Ueno, M., and M. Kunii, 2009: Some aspects of azimuthal wavenumber-one structure of typhoons represented in the JMA operational mesoscale analyses. *J. Meteor. Soc. Japan,* **87,** 615–633.

——, and K. Bessho, 2011: A statistical analysis of near-core surface wind asymmetries in typhoons obtained from QuikSCAT data. *J. Meteor. Soc. Japan,* **89,** 225–241.

Uhlhorn, E. W., and P. G. Black, 2003: Verification of remotely sensed sea surface winds in hurricanes. *J. Atmos. Oceanic Technol.,* **20,** 99–116.

——, and D. S. Nolan, 2012: Observational undersampling in tropical cyclones and implications for estimated intensity. *Mon. Wea. Rev.,* **140,** 825–840.

——, P. G. Black, J. L. Franklin, M. Goodberlet, J. Carswell, and A. S. Goldstein, 2007: Hurricane surface wind measurements from an operational Stepped Frequency Microwave Radiometer. *Mon. Wea. Rev.,* **135,** 3070–3085.

Velden, C., and Coauthors, 2006: The Dvorak tropical cyclone intensity estimation technique: A satellite-based method that has endured for over 30 years. *Bull. Amer. Meteor. Soc.,* **87,** S6–S9.

Vukicevic, T., E. W. Uhlhorn, P. Reasor, and B. Klotz, 2014: A novel multiscale intensity metric for evaluation of tropical cyclone intensity forecasts. *J. Atmos. Sci.,* in press.

Wang, Y., and G. J. Holland, 1996: Tropical cyclone motion and evolution in vertical shear. *J. Atmos. Sci.,* **53,** 3313–3332.

Wingo, M. T., and D. J. Cecil, 2010: Effects of vertical wind shear on tropical cyclone precipitation. *Mon. Wea. Rev.,* **138,** 645–662.

Wu, L., S. A. Braun, J. Halverson, and G. Heymsfield, 2006: A numerical study of Hurricane Erin (2001). Part I: Model verification and storm evolution. *J. Atmos. Sci.,* **63,** 65–86.

Xie, L., S. Bao, L. J. Pietrafesa, K. Foley, and M. Fuentes, 2006: A real-time hurricane surface wind forecasting model: Formulation and verification. *Mon. Wea. Rev.,* **134,** 1355–1370.

Zhang, J., and E. W. Uhlhorn, 2012: Hurricane sea surface inflow angle and an observation-based parametric model. *Mon. Wea. Rev.,* **140,** 3587–3605.